Jet launching from merging magnetized binary neutron stars with realistic equations of state

Milton Ruiz[1], Antonios Tsokaros[1], and Stuart L. Shapiro[1,2]

[1]*Department of Physics, University of Illinois at Urbana-Champaign, Urbana, Illinois 61801, USA*
[2]*Department of Astronomy & NCSA, University of Illinois at Urbana-Champaign,*
Urbana, Illinois 61801, USA

We perform general relativistic, magnetohydrodynamic (GRMHD) simulations of binary neutron stars in quasi-circular orbit that merge and undergo delayed or prompt collapse to a black hole (BH). The stars are irrotational and modeled using an SLy or an H4 nuclear equation of state. To assess the impact of the initial magnetic field configuration on jet launching, we endow the stars with a purely poloidal magnetic field that is initially unimportant dynamically and is either confined to the stellar interior or extends from the interior into the exterior as in typical pulsars. Consistent with our previous results, we find that only the BH + disk remnants originating from binaries that form hypermassive neutron stars (HMNSs) and undergo delayed collapse can drive magnetically powered jets. We find that the closer the total mass of the binary is to the threshold value for prompt collapse, the shorter is the time delay between the gravitational wave peak amplitude and jet launching. This time delay also strongly depends on the initial magnetic field configuration. We also find that seed magnetic fields confined to the stellar interior can launch a jet over ~ 25 ms later than those with pulsarlike magnetic fields. The lifetime of the jet [$\Delta t \lesssim 150$ ms] and its outgoing Poynting luminosity [$L_{\rm EM} \sim 10^{52 \pm 1}$ erg/s] are consistent with typical short gamma-ray burst central engine lifetimes, as well as with the Blandford–Znajek mechanism for launching jets and their associated Poynting luminosities. Our numerical results also suggest that the dynamical ejection of matter can be enhanced by the magnetic field. Therefore, GRMHD studies are required to fully understand kilonova signals from GW170818-like events.

I. INTRODUCTION

The coincident detection of gravitational waves (GWs) with counterparts across the electromagnetic (EM) spectrum from GW170817, whose source has been officially classified as a merging binary neutron star [1–3], triggered the beginning of multimessenger astronomy. This single multimesssenger event provides: (i) the first direct evidence that compact binary mergers where at least one of the companions is a neutron star can be the progenitors of the central engine that powers short gamma-ray bursts (sGRBs). This conclusion was anticipated in [4–6] and confirmed by self-consistent simulations in full general relativity, magnetohydrodynamics (GRMHD) of merging binary neutron stars (NSNSs) [7,8], and binary black hole-neutron stars (BHNSs) [9,10]; (ii) tight constraints on the equation of state (EOS) at supranuclear densities [11,12]; (iii) limits to the maximum mass of neutron stars [13–16]; (iv) evidence of ejecta masses of ≈ 0.01–$0.05 \ M_\odot$ with velocities ≈ 0.1–0.3 c [17–19]. This ejecta is roughly consistent with the estimated r-process production rate required to explain the Milky Way r-process abundances; and (v) an independent measure for the expansion of the Universe [20,21]. GW170817 also demonstrated that to

understand multimessenger observations and, in particular, to understand the physics of matter under extreme conditions, it is crucial to compare them to predictions from theoretical modeling. Due to the complexity of the underlying physical phenomena, such modeling is largely numerical in nature.

Our GRMHD numerical simulations in [7–10], which model the NSs by a simple $\Gamma = 2$, polytropic EOS, provided an existence proof for jet launching.[1] However, to date there are no self-consistent, GRMHD calculations of NSNS or BHNS mergers involving realistic EOSs, or detailed microphysical processes, confirming these results. Such jets are believed to be crucial for launching a GRB (see e.g., [22–24]). The numerical studies of NSNS mergers undergoing delayed collapse to a BH reported in [25,26], in which different EOSs, mass ratios, and orientations of a poloidal magnetic field confined to the stellar interior, were explored found no evidences of magnetically driven

---

[1]We define an incipient jet as a tightly collimated, mildly relativistic outflow which is driven by a tightly wound, helical, forcefree magnetic field (i.e., $B^2/(8\pi\rho_0) \gg 1$, where ρ_0 is the rest-mass density, and $B^2 = B_i B^i$, with B^i the magnetic field [9].)

outflows or incipient jets, though their results confirm the formation of an ordered magnetic field above the BH poles (see e.g., Fig. 7 in [25]). It is likely that longer evolutions and/or higher resolutions are required to properly capture the undergoing magnetic instabilities for the emergence of an incipient jet. The formation of jet-like structures have been also reported in [27]. On the other hand, the very high resolution studies of NSNS mergers in [28] found no jets nor an ordered poloidal field above the BH poles after ~ 39 ms following merger. By t ~ 26 ms following BH formation, there is still material in the atmosphere that is being accreted, so that the strong ram pressure of the fall-back debris chokes the emergence of a magnetically driven outflow. An incipient jet might be launched once the baryon-loaded surrounding debris above the BH poles becomes sparse. However, the emergence of an incipient jet may be possible only for EOSs for which the fall-back timescale is shorter than the accretion disk lifetime [29]. On the other hand, microphysical processes may also have strong impact on the final outcome of compact binary mergers and jets (see e.g., [30,31]). For example, neutrino processes in BH + disk systems may extract a significant amount of energy from inner regions of disk to power jets [32–36]. However, they cannot explain the duration of typical sGRBs (see e.g., [36,37]). Nevertheless, it has been suggested that, in slow spinning BH + disk systems, jets can be initially triggered by neutrino pair annihilation and then powered by the Blandford-Znajek (BZ) mechanism [38,39], leading to a transition from a thermally dominated fireball to a Poynting dominated outflow, as observed in some GRBs such as GRB 160625B [40].

As a crucial step in solidifying the role of NSNSs as multimessenger sources, we survey in this paper configurations that undergo either delayed or prompt collapse and treat different representative EOSs and initial geometries of their magnetic field to probe their impact on jet launching and the dynamical ejection of matter. In particular, the NSs are modeled using a piecewise polytropic representation of the nuclear SLy [41] and H4 EOSs [42], as in [43]. We adopt these as representative of realistic candidate EOSs that are broadly consistent with current data [44–46]. For comparison, we also consider the binaries we considered in [7,8,47] in which the stars are modeled using a simple polytropic EOS with $\Gamma = 2$. For the magnetic field, we endow the stars initially with a purely poloidal magnetic field that either extends from the interior of the NSs into its exterior, as in pulsars, or that is confined to the stellar interior. We also evolve unmagnetized configurations to assess the impact of the magnetic field on the ejecta. As NSNS mergers tend to create very baryon-loaded environments (see e.g., [36,48]), we consider binaries whose merger outcome is a short- ($1 \lesssim \tau_{HMNS} \lesssim 5$ ms), medium- ($5 \lesssim \tau_{HMNS} \lesssim 20$ ms) or long-lived ($\tau_{HMNS} \gtrsim 20$ ms) hypermassive neutron star (HMNS) followed by delayed collapse to a BH. These choices will allow us to probe the impact of light vs heavy matter

environments on the physical properties of the incipient jet. Here τ_{HMNS} is the lifetime of the HMNS.

Consistent with our results reported in [7,8], we find that incipient jets only emerge from binary remnants that undergo delayed collapse, regardless of the EOS. The lifetime of the jet [$\Delta t \sim 92$–150 ms] and its corresponding outgoing EM Poynting luminosity [$L_{EM} \sim 10^{52 \pm 1}$ erg/s] are consistent with the lifetime of the sGRB central engine [49–52], as well as with the Blandford-Znajek (BZ) mechanism for launching jets and their associated Poynting luminosities [39]. Our results can be summarized as follows: (i) the closer the total mass of the binary is to the threshold value for prompt collapse, the shorter is the time delay between the GW peak amplitude (our definition of the moment of coalescence) and the jet launching time. In particular, we find that the BH + disk remnant of a stiff H4 NSNS configuration in which $\tau_{HMNS} \sim 2.5$ ms (labeled as H4M3.0P in the discussion below) launches an incipient jet after ~ 19 ms following BH formation, while that of an H4 NSNS configuration in which $\tau_{HMNS} \sim 9.6$ ms (labeled H4M2.8P) launches a jet after ~ 27 ms following BH formation; (ii) the jet launching time strongly depends on the initial geometry of the seed magnetic field. We observe that the BH + disk remnant of a soft SLy binary initially endowed with a pulsarlike poloidal magnetic field (labeled as SLyM2.7P) launches an incipient jet at t ~ 20 ms following BH formation, while the same binary endowed with a poloidal magnetic field confined to the stellar interior (labeled SLyM2.7I) launches it at t ~ 60 ms following BH formation. As we discuss later, during the BH + disk phase the magnetic energy in the latter is a factor of ~ 20 times smaller than in the former. Therefore, the BH + disk remnant in SLyM2.7I requires more time for magnetic pressure gradients to overcome the ram-pressure of the falling-back debris and eventually launch an incipient jet. On the other hand, in the prompt collapse case, the absence of an extended HMNS epoch prevents the magnetic field from reaching equipartition strength above the remnant BH poles, thereby preventing magnetic field collimation and a magnetically supported outflow; (iii) the dynamical ejection of matter following merger strongly depends on the initial magnetic field geometry. Note that it has been suggested that the magnetic field lines of a rotating compact object may accelerate fluid elements due to a magnetocentrifugal mechanism [53]. These results suggest that magnetic field is a key ingredient in explaining kilonova signatures from GW170817-like events. We use an analytical model recently derived in [54] to compute the peak EM luminosity, the rise time and an effective temperature of the potential kilonova. We find that the bolometric luminosity is $L_{knova} = 10^{40.6 \pm 0.5}$ erg/s with rise times $\tau_{peak} \sim 0.4$–5.1 days and an effective temperature $T_{peak} \sim 10^{3.5}$ K. This temperature can be translated in a peak wavelength $\lambda_{peak} = 1.35 \times 10^3$ nm$(T_{peak}/10^{3.33}$ K$)^{-1}$ [54], implying $\lambda_{peak} \sim 730$–1830 nm. The associated

emission may be detected with current or planned telescopes such as ALMA or the Vera C. Rubin Observatory [55,56]; and finally (iv) using the GW match function (see e.g., [57]), we find that the imprints of the magnetic field on the gravitational radiation can be observed by current based-ground detectors (aLIGO/Virgo/KAGRA) only if the GW event occurs within at a distance $\lesssim 6.0$ Mpc. We recall that GW170817, the closest GW signal detected to date, had a luminosity distance of 40^{+8}_{-14} Mpc [1]. If the GW event occurs within a distance $\lesssim 50$ Mpc, these imprints can be observed only with next generation of GW observatories, such as the Einstein Telescope or Cosmic Explorer (see e.g., [58]), with a sigma-to-noise ratio (SNR) $\gtrsim 30$.

The remainder of the paper is organized as follows. A short summary of the numerical methods and their implementation is presented in Sec. II A. A detailed description of the adopted initial data and the grid structure used to evolve the GRMHD equations numerically are given in Sec. II B and Sec. II C, respectively. A suite of diagnostics used to verify the reliability of our numerical calculations is summarized in Sec. II D. We present our results in Sec. III. Finally, we summarize our findings and conclusions in Sec. IV. Throughout the paper we adopt geometrized units ($G = c = 1$) except where stated explicitly. Greek indices denote all four spacetime dimensions, while Latin indices imply spatial parts only.

II. NUMERICAL SETUP

A. Methods

Much of the numerical approach employed here has been extensively discussed in previous works (see e.g., [7,59,60]). Therefore, in the following we only summarize the basics aspects, referring the reader to those references for further details and code tests.

We use our well-tested ILLINOIS GRMHD code [61] which is embedded on the CACTUS infrastructure [62] and employs the CARPET code [63,64] for its moving-box mesh capability. Our code evolves the Baumgarte–Shapiro–Shibata–Nakamura (BSSN) equations [65,66], coupled with puncture gauge conditions cast in first order form (see Eq. (2)–(4) in [67]), using fourth order centered spatial differencing, except on shift advection terms, where a fourth order upwind differencing is used. Fifth order Kreiss-Oliger dissipation [68] is also added in the BSSN evolution equations. The matter and magnetic fields are evolved using the equations of ideal GRMHD, which are cast in a conservative scheme, via a high-resolution shock capturing method (see Eqs. (27)–(29) in [61]). To ensure the magnetic field remains divergenceless during the whole evolution, we integrate the magnetic induction equation using a vector potential $\mathcal{A}^{\mu}$ (see Eqs. (19)–(20) in [61]). We adopt the generalized Lorenz gauge described in [69] to avoid the build up of spurious magnetic fields [70]. The time integration is performed via the method of lines

using a fourth-order accurate Runge-Kutta integration scheme with a Courant-Friedrichs-Lewy (CFL) factor set to 0.5.

B. Initial data

1. Equation of state (EOS)

We consider NSNS configurations in a quasiequilibrium circular orbit that inspiral, merge and undergo either delayed or prompt collapse to a BH. The binaries consist of two identical irrotational NSs, modeled by a piecewise polytropic representation of the nuclear EOSs SLy (soft) [41] and H4 (stiff) [42], as in [43]. The initial binary data are computed using the compact object calculator (COCAL) [71,72], and their properties are summarized in Table I.

We note that these representative EOSs broadly satisfy the current observational constraints on NSs. For example, the maximum mass configuration of an isolated star predicted by SLy is $M^{\max}_{\mathrm{sph}} = 2.06\ M_{\odot}$, while that predicted by H4 is $M^{\max}_{\mathrm{sph}} = 2.03\ M_{\odot}$. Both are consistent with: (i) $M^{\max}_{\mathrm{sph}} > 2.072^{+0.067}_{-0.066}\ M_{\odot}$ from the NICER and XMM analysis of PSR J0740 + 6620 [73]; (ii) $M^{\max}_{\mathrm{sph}} > 2.01^{+0.017}_{-0.017}\ M_{\odot}$ from the NANOGrav analysis of PSR J1614-2230 [44]; (iii) $M^{\max}_{\mathrm{sph}} > 2.01^{+0.14}_{-0.14}\ M_{\odot}$ from the pulsar timing analysis of PSR J0348 + 0432 [45]; and $M^{\max}_{\mathrm{sph}} > 2.14^{+0.20}_{-0.18}\ M_{\odot}$ from the NANOGrav and the Green Bank Telescope [46]. We also note that SLy predicts that a star with a mass of 1.4 $M_{\odot}$ has a radius of R = 11.46 km, consistent with the value R = $11.94^{+0.76}_{-0.87}$ km obtained by a combined analysis of x-ray and GW measurements of PSR J0740 + 6620 [74]. Such a star modeled with a H4 EOS has a radius of R = 13.55 km, which is just marginally outside of the above constraint. Consistent with this, the combined

TABLE I. Summary of the initial properties of the NSNS configurations. We list the EOS employed to model the NSs, the rest-mass M_0, the equatorial coordinate radius R_x toward the companion of each star, the compactness $\mathcal{C}$ and the tidal deformability $\Lambda = (2/3)k_2\mathcal{C}^{-5}$ (where k_2 is the second Love number), the ADM mass M, and the angular velocity Ω, for an initial binary coordinate separation of ~45 km. The tag for each configuration is composed of the EOS followed by the binary ADM mass. We also consider the $\Gamma = 2$ NSNS configurations treated previously in [7,8,47].

Model	EOS	$M_0[M_\odot]$	R_x [km]	$\mathcal{C}$	Λ	$M[M_\odot]$	$M\Omega$
SLyM2.6	SLy	1.45	9.14	0.169	463	2.6	0.024
SLyM2.7	SLy	1.51	9.04	0.175	367	2.7	0.023
SLyM3.0	SLy	1.71	8.72	0.197	173	3.0	0.031
H4M2.8	H4	1.55	11.12	0.155	818	2.8	0.025
H4M3.0	H4	1.67	10.81	0.166	524	3.0	0.031
Γ2M2.8	$\Gamma = 2$	1.51	12.74	0.140	979	2.8	0.027
Γ2M3.0	$\Gamma = 2$	1.67	11.52	0.160	359	3.0	0.030

analysis of the LIGO/Virgo scientific collaboration (LVSC) of the progenitors of GW170817 with the radio-timing observations of the pulsar J0348 + 0432 [11,45] constrain the radius of a NS with mass in the range 1.16–1.6 $M_\odot$ to be $11.9^{+1.4}_{-1.4}$ km at the 90% credible level. However, the NICER analysis of PSR J0030 + 0451 [75] constrains the radius of a NS with mass of $1.44^{+0.15}_{-0.14}$ $M_\odot$ to be R = $13.02^{+1.24}_{-1.06}$ km. SLy and H4 EOSs predict that a 1.44 $M_\odot$ star has a radius of 11.45 km and 13.54 km, respectively. The former is hence slightly below the NICER constraint. Furthermore, the LVSC analysis of GW170817 predicts that the tidal deformability of a 1.4 $M_\odot$ NS is $\Lambda_{1.4} = 190^{+390}_{-120}$ at the 90% credible level [11]. Such a star has $\Lambda_{1.4} = 306.4$ and $\Lambda_{1.4} = 886.6$ for SLy and H4, respectively. Therefore, the NICER analysis favors stiff (e.g., H4) over soft EOSs (e.g., SLy), while that of the LVSC favors soft over stiff EOSs [76].

For comparison, we also consider the $\Gamma = 2$ NSNS configurations we treated previously in [7,8,47] that allow us to cover a large set of stellar compactions. Note that $\Gamma = 2$ is the stiffest EOS considered in this survey. When using an Γ-law EOS, we have the freedom to scale the masses and distance to any value. Therefore, we rescale the rest-mass of the $\Gamma = 2$ star companions to match those of SLyM2.7 (i.e., $M_0 = 1.51 M_\odot(\kappa/\kappa_L)^{1/2}$, where $\kappa_L = 232.93$ km^2 is the polytropic constant employed to compute the initial data). We note that the maximum mass predicted by the $\Gamma = 2$ EOS is $M_{sph}^{max} = 1.69(k/k_L)^{1/2} M_\odot$ and, that a $\Gamma = 2$ star with a mass of 1.4 $M_\odot$ has a radius of $R = 22.72(k/k_L)^{1/2}$ km.

The NSNS merger outcome may be a remnant that can either settle into a transient HMNS or promptly form a highly spinning BH upon merger. Given an EOS, this outcome depends strongly on the total mass of the binary and it is independent of the mass-ratio [77]. The threshold mass M^{thres} for prompt collapse for a $\Gamma = 2$ EOS is $\simeq 2.88(k/k_L)^{1/2} M_\odot$, while for SLy and H4 EOSs are $M^{thres} \simeq 2.82 M_\odot$ and $M^{thres} \simeq 3.12 M_\odot$, respectively [78]. Thus, it is expected that only the NSNS configurations SLyM3.0 and Γ2M3.0 (see Table I) undergo prompt collapse to a BH. The merger outcome in all other cases is a highly differentially rotating HMNS [79].

A cold EOS is adequate to model the NS prior to merger. However, during merger considerable shock heating increases the internal energy. To account for this, we adopt an EOS that has both a thermal and cold contribution. The total pressure can be expressed as

$$P = P_{th} + P_{cold}, \qquad (1)$$

where $P_{cold} = \kappa_i \rho_0^{\Gamma_i}$, with κ_i and Γ_i the corresponding polytropic constant and the polytropic exponent in the rest-mass density range $\rho_{0,i-1} \leq \rho_0 \leq \rho_{0,i}$, respectively (see e.g., [43]), and the thermal pressure is given by

$$P_{th} = (\Gamma_{th} - 1)\rho_0(\epsilon - \epsilon_{cold}), \qquad (2)$$

where

$$\epsilon_{cold} = -\int P_{cold}d(1/\rho_0), \qquad (3)$$

and Γ_{th} a constant that we set to $1.66 \simeq 5/3$ in all our simulations. This value is appropriate for ideal nonrelativistic baryons [80,81].

We further simplify our notation hereafter by dropping the factor (k/k_L) in all physical quantities quoted for $\Gamma = 2$ models. The scalefree property of these results can be easily recovered by restoring this factor.

2. Magnetic field configuration

Following [7], we initially seed the star with a dynamically unimportant, purely poloidal magnetic field that extends from the interior of the NSs into the exterior (see top right panel in Fig. 1), and that approximately corresponds to that generated by an interior current loop with radius r_0 and current I_0 (see Eq. (6) in [8]). In all our configurations, we choose I_0 and r_0 such that the maximum value of the magnetic-to-gas-pressure ratio in the NS interior is $P_{mag}/P_{gas} = 0.003125$. The resulting magnetic field strength at the NS pole measured by a normal observer is $B_{pole} \simeq 10^{15.3}$ G. This choice allows us to mimic the exponential growth of the magnetic field observed in high-resolution simulations arising from magnetic instabilities (mainly the Kelvin-Helmholtz (KH) instability) triggered during the binary merger. The NSNS simulations reported in [82] found that, with a local numerical resolution of $\Delta x \sim 37$ m, a pure poloidal magnetic field confined in the NSs with a strength of $\sim 10^{11}$ G can be amplified to rms values of $\sim 10^{16}$ G within the first ~ 5 ms following merger. Similar results have been reported in very-high-resolution NSNS simulations in [83] employing a local resolution of $\Delta x \sim 17.5$ m. These values are beyond the resolutions of this broad survey (see Table II).

To reliably evolve the exterior magnetic field and simultaneously model magnetic-pressure dominance that characterizes the force-free pulsar-like magnetosphere, we initially enforced a variable and low atmosphere in regions where magnetic field stresses dominate over the fluid pressure gradient such that the magnetic-to-gas-pressure ratio in the NS exterior is $P_{mag}/P_{gas} = 100$ (see Eq. (4) in [10] for implementation details). This choice increases the total rest-mass of the system in less than 0.5%.

Finally, to assess the impact of the initial magnetic field configuration, and to compare with previous studies, we also consider cases where seed the NSs with a poloidal magnetic field confined to the stellar interior. This field is generated via the vector potential A_ϕ [84]
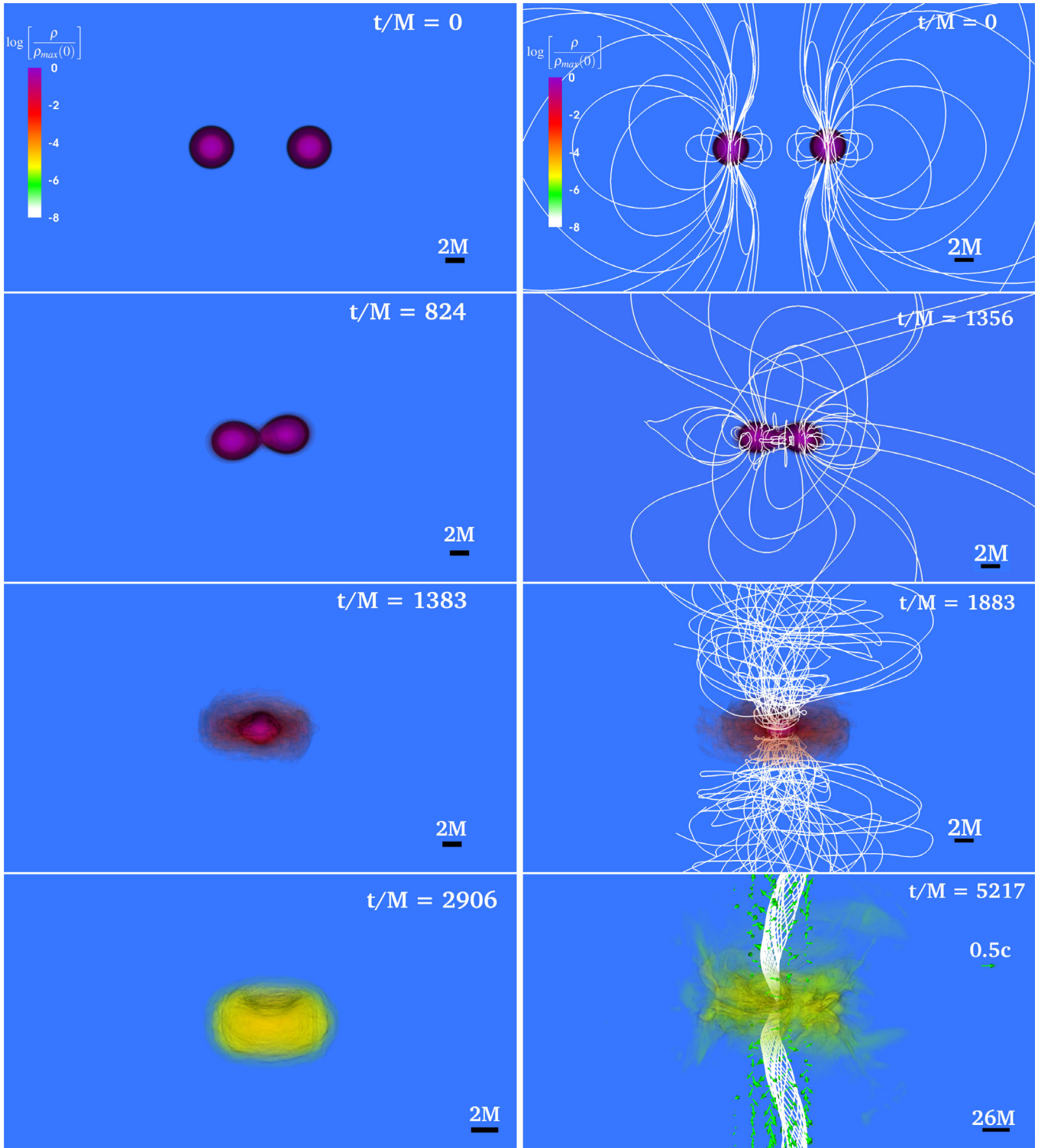
FIG. 1.   Volume rendering of the rest-mass density ρ_0 normalized to its initial NS maximum value (log scale) at selected times for H4M2.8H (left column) and SLyH2.6P (right column) cases (see Table III). White lines shows the magnetic field lines and the arrows indicate plasma velocities. The bottom right panel highlights the system after an incipient jet is launched. Here M = 2.8 $M_\odot$ (left column) or M = 2.6 $M_\odot$ (right column), hence $M \sim 1.3 \times 10^{-2}$ ms ~ 4 km.

TABLE II. Grid hierarchy for models listed in Table I. The computational mesh consists of two sets of nine nested refinement boxes for the binaries modeled with a nuclear EOS, and seven nested refinement boxes for those modeled with a $\Gamma = 2$ EOS. The finest boxes are centered on each star and have a half-length of $\sim 1.2 R_{\mathrm{NS}}$, where R_{NS} is the initial equatorial stellar radius. The number of grid points covering the equatorial radius of NS is denoted by N_{NS}. In terms of grid points per NS radius, the resolution used here is a factor of ~ 1.4 finer than that in [7]. In all cases, we impose reflection (equatorial) symmetry about the orbital plane.

Model	Grid Hierarchy[a]	Maximum resolution	N_{NS}
SLyM2.6	2835.26 km/2^{n-1}	110.75 m	83
SLyM2.7	2835.26 km/2^{n-1}	110.75 m	82
SLyM3.0	2835.26 km/2^{n-1}	110.75 m	79
H4M2.8	3477.92 km/2^{n-1}	92 m	121
H4M3.0	3477.92 km/2^{n-1}	92 m	118
Γ2M2.8[b]	1015.02 km/2^{n-1}	206.27 m	62
Γ2M3.0[b]	954.06 km/2^{n-1}	133.10 m	87

[a]Box half-length.
[b]Configurations treated previously in [7,8,47].

$$\mathcal{A}_i = \left(-\frac{y - y_c}{\varpi_{\mathrm{c}}^2} \delta^x_{\ i} + \frac{x - x_c}{\varpi_{\mathrm{c}}^2} \delta^y_{\ i} \right) \mathcal{A}_\varphi, \qquad (4)$$

$$\mathcal{A}_\varphi = \mathcal{A}_b \varpi_{\mathrm{c}}^2 \max(P_{\mathrm{gas}} - P_{\mathrm{cut}}, 0)^{n_b}, \qquad (5)$$

where $(x_{\mathrm{c}}, y_{\mathrm{c}}, 0)$ is the coordinate position of the center of mass of the NS, $\varpi_{\mathrm{c}}^2 = (x - x_{\mathrm{c}})^2 + (y - y_{\mathrm{c}})^2$, and A_b, n_p and P_{cut} are free parameters. The cutoff pressure parameter P_{cut} confines the magnetic field inside the NS within the region where $P_{\mathrm{gas}} > P_{\mathrm{cut}}$. The parameter n_b determines the degree of central condensation of the magnetic field. In our evolutions, we choose P_{cut} to be 1% of the maximum pressure and $n_b = 1$, while the value of A_b is chosen such as the magnetic-to-gas-pressure ratio at the NS center matches that in our pulsarlike case (i.e., $P_{\mathrm{mag}}/P_{\mathrm{gas}} = 0.003125$).

C. Grid structure

The numerical grid hierarchy is summarized in Table II. It consists of two sets of nested refinement boxes centered on each star. Each of them contains nine boxes that differ in size and in resolution by factors of two. When two boxes overlap they are replaced by a common box centered on the center of mass of the NSNS. The finest box around the NS has a side half-length of $\sim 1.2R$, where R is the initial NS equatorial radius. This choice allows us to initially resolve the equatorial NS radius by ~ 120 grid points (see Table I). We impose reflection (equatorial) symmetry across the orbital plane. In terms of grid points per NS radius, the resolution employed in these studies is a factor of

~ 1.4 finer than that in [7,8] where NSNSs are modeled by a $\Gamma = 2$ EOS (see Table I).

D. Diagnostics

To validate our evolutions, we monitor the L_2 norm of the normalized Hamiltonian and momentum constraints computed through Eqs. (40)–(43) in [67]. In all simulations, the Hamiltonian constraint violations remain smaller than 0.06% during the inspiral, peak at $\sim 0.3\%$ during BH formation and then relax to $\sim 0.02\%$ once the BH + disk remnant settles into a steady state. The normalized momentum constraint violations remain smaller than 0.8% during the inspiral, peak at 4.2% during BH formation and subsequently relax to $\sim 0.18\%$ during steady state. We note that these values are similar to those previously reported in our long-term, pure hydrodynamic simulations of spinning NSNSs modeled by SLy and ALF2 EOSs [85].

After the catastrophic collapse of the merger-outcome-remnant, we use the `AHFinderDirect` thorn [86] to track the BH apparent horizon. In addition, we estimate the BH mass M_{BH} and its dimensionless spin a/M_{BH} using the isolated horizon formalism as in [87]. We use the `Psikadelia` thorn to compute the Weyl scalar Ψ_4 which is decomposed into $s = -2$ spin-weighted spherical harmonic modes. We use Eqs. (2.8), (2.11) and (2.13) in [88] at ten different extraction radii between $r_{\mathrm{min}} \approx 50\ M$ and $r_{\mathrm{max}} \approx 320\ M$ to compute the total flux of energy and angular momentum transported away by GWs. We find that between $\sim 0.15\%$ and $\sim 2.3\%$ of the total energy of our NSNS models is radiated away during the evolution in form of gravitational radiation, while between $\sim 8.7\%$ and $\sim 17.4\%$ of the angular momentum is radiated (see Table III). We measure the dynamical ejection of matter via $M_{\mathrm{esc}} = \int_{r > r_0} \rho_* d^3 x$, where $\rho_* = -\sqrt{\gamma} \rho_0 n_\mu u^\mu$, on the conditions that: (i) the specific energy $E = -u_t - 1$ of the outgoing material is always positive (unbound material), and (ii) the radial velocity of the outgoing material $v^r > 0$. Here γ is the determinant of the three-metric, n_μ is the timelike future pointing unit (i.e., normal) vector, and u^μ is the four-velocity of the fluid. We vary the coordinate radius r_0 between $r_{\mathrm{min}} = 30\ M$ and $r_{\mathrm{max}} = 100\ M$ to verify that the measure of the ejecta is r_0-independent. Depending on the stiffness of the EOS and the magnetic field we find that the rest-mass ejected following merger ranges between $\lesssim 10^{-4}\ M_\odot$ and $\sim 10^{-2}\ M_\odot$ consistent with values previously reported in e.g., [89,90]. We note that if ejected material with masses $\gtrsim 10^{-2}\ M_\odot$ is converted to r-process elements, GW170817-like events could account for the amount of heavy elements observed in the Milky Way [91,92].

We monitor the conservation of the ADM mass and ADM angular momentum computed throughout Eqs. (19)–(22) in [84]. Consistent with [85], in all our evolved configurations we find that the ADM mass is

TABLE III. Summary of key results. Here t_{GW}, Δt_{BH} and t_{sim} are the merger time at GW peak amplitude, the BH formation time measured as $t_{BH} - t_{GW}$, and the full simulation time, respectively, all in ms. The mass and the dimensionless spin parameter of the BH remnant are given by $M_{BH}[M_\odot]$ and $\tilde{a} = a_{BH}/M_{BH}$, both computed using the isolated horizon formalism. $M_{disk}[M_\odot]$ denotes the rest-mass of the accretion disk, $\dot{M}[M_\odot/s]$ is the rest-mass accretion rate computed via Eq. (A11) in [93]. These two quantities are measured when $\dot{M}$ begins to settle into a steady state. The disk lifetime is $\tau_{disk}[ms] \equiv M_{disk}/\dot{M}$, M_{esc} denotes the rest-mass fraction of escaping matter (ejecta) following GW peak amplitude. The fraction of energy and angular momentum carried off by gravitational radiation are given by $\Delta \bar{E}_{GW} \equiv \Delta E_{GW}/M_{ADM}$ and $\Delta \bar{J}_{GW} \equiv \Delta J_{GW}/J_{ADM}$, respectively. α_{SS} is the Shakura–Sunyaev viscosity parameter, $B_{rms}[G]$ is the rms value of the magnetic field at the HMNS pole just before collapse. The Poynting luminosity driven by the jet, and time-averaged over the last ~5 ms before the termination of our simulations, is denoted as $L_{EM}[erg/s]$. Γ_L denotes the maximum fluid Lorentz factor at t_{sim}. $L_{knova}[erg/s]$, $\tau_{peak}[days]$, and $T_{peak}[K]$ are the peak EM luminosity, the rise time, and the temperature of the potential kilonova, respectively, and finally, the fate of the binary merger. An "P", "I" or "H" at the end of the tag name for each configuration denotes the initial magnetic field configuration, i.e., P = pulsar-like (interior + exterior) magnetic field, I = interior magnetic field, or H = hydrodynamic (unmagnetized). Center dots denote "not applicable".

Model	t_{GW}	Δt_{BH}	t_{sim}	M_{BH}	$\tilde{a}$	$M_{disk}/M_0^{(a)}$ $\times 10^{-2}$	$\dot{M}$	τ_{disk}	M_{esc}/M_0 $\times 10^{-2}$	$\Delta \bar{E}_{GW}$ $\times 10^{-2}$	$\Delta \bar{J}_{GW}$ $\times 10^{-2}$	α_{SS}	B_{rms}	L_{EM}	Γ_L	L_{knova}	τ_{peak}	T_{peak}	Fate
SLyM2.6P	17.5	41.0	68.6	2.26	0.47	8.71	1.93	130.88	0.870	1.51	13.80	0.01–0.04	$10^{16.2}$	$10^{52.3}$	1.24	$10^{40.7}$	1.61	$10^{3.4}$	HMNS→delayedcol
SLyM2.6H	17.6	...	60.0	...	...	...	...	...	0.870	2.34	17.38	...	...	...	...	$10^{40.8}$	1.67	$10^{3.4}$	HMNS→delayedcol
SLyM2.7P	15.7	8.9	48.2	2.45	0.62	6.16	2.01	92.55	0.251	2.19	15.49	0.02–0.07	$10^{16.0}$	$10^{52.8}$	1.26	$10^{41.2}$	5.13	$10^{3.2}$	HMNS→delayedcol
SLyM2.7I	15.8	8.2	100.2	2.50	0.69	3.08	0.96	96.89	0.501	1.78	13.49	0.01–0.03	$10^{15.8}$	$10^{51.3}$	1.25	$10^{40.9}$	2.31	$10^{3.3}$	HMNS→delayedcol
SLyM2.7H	14.6	9.0	32.0	2.51	0.70	2.24	0.94	71.97	0.316	2.19	15.13	...	...	...	...	$10^{40.8}$	1.91	$10^{3.4}$	HMNS→delayedcol
SLyM3.0P	11.5	0.6	24.4	2.96	0.81	0.25	$10^{-2.4}$	...	0.050	0.89	9.55	...	$10^{16.1}$	$10^{45.7}$	...	$10^{40.5}$	0.93	$10^{3.5}$	Prompt collapse
SLyM3.0H	11.5	0.6	23.5	2.95	0.80	0.40	$10^{-2.3}$	...	0.013	0.89	9.55	...	...	...	...	$10^{40.3}$	0.47	$10^{3.6}$	Prompt collapse
H4M2.8P	11.5	9.6	56.3	2.64	0.71	3.50	1.11	97.75	1.000	1.66	13.49	0.01–0.09	$10^{15.9}$	$10^{52.5}$	1.30	$10^{41.1}$	3.20	$10^{3.3}$	HMNS→delayedcol
H4M2.8I	11.5	13.3	46.5	2.69	0.73	2.21	1.20	57.10	0.063	1.51	12.59	0.02–0.04	$10^{15.7}$	...	...	$10^{40.6}$	0.85	$10^{3.5}$	HMNS→delayedcol
H4M2.8H	11.5	9.1	40.2	2.70	0.73	1.51	0.37	120.65	0.016	1.78	13.80	...	...	...	...	$10^{40.4}$	0.43	$10^{3.6}$	HMNS→delayedcol
H4M3.0P	9.70	2.5	40.0	2.93	0.80	1.04	0.23	152.23	0.016	0.98	8.91	$10^{-3.5}$–0.02	$10^{16.0}$	$10^{52.2}$	1.19	$10^{40.4}$	0.43	$10^{3.6}$	HMNS→delayedcol
H4M3.0H	9.70	2.6	34.8	2.95	0.81	0.54	0.19	94.50	0.016	0.91	8.71	...	...	...	...	$10^{40.4}$	0.42	$10^{3.5}$	HMNS→delayedcol
Γ2M2.8P(b)	6.9	16.9	70.0	2.65	0.74	2.82	0.48	92.43	...	0.79	12.59	0.04–0.08	$10^{15.9}$	$10^{51.3}$	1.25	...	...	...	HMNS→delayedcol
Γ2M2.8H(b)	7.2	14.5	48.8	2.65	0.73	0.98	0.48	74.86	0.012	1.29	16.98	...	...	...	...	$10^{40.4}$	0.38	$10^{3.6}$	HMNS→delayedcol
Γ2M3.0P(b)	4.2	0.51	15.0	2.80	0.83	0.47	0.34	...	...	0.78	12.30	...	$10^{15.9}$	...	...	...	...	...	Prompt collapse

a M_0 denotes the initial total rest-mass of the system.
b Configurations treated previously in [7,8,47].

conserved to within $\lesssim 1\%$ and angular momentum to within $\lesssim 6\%$. In addition, we monitor the conservation of the rest mass $M_0 = \int \rho_* d^3 x$, which is conserved to within $\lesssim 0.05\%$, as well as the magnetic energy growth outside the BH apparent horizon $\mathcal{M} = \int u^\mu u^\nu T_{\mu\nu}^{(\mathrm{EM})} dV$ as measured by a comoving observer [8].

To probe MHD turbulence in our systems, we compute the effective Shakura–Sunyaev α_{SS} parameter [94] associated with the effective viscosity due to magnetic stresses $\alpha_{\mathrm{SS}} \sim T_{\hat{r}\hat{\phi}}^{\mathrm{EM}}/P$ (see Eq. (26) in [95]). To check if the magnetorotational instability (MRI) can be captured in our evolution following the NSNS merger, we compute the λ_{MRI}-quality factor $Q_{\mathrm{MRI}} \equiv \lambda_{\mathrm{MRI}}/dx$, which measures the number of grid points per fastest growing MRI mode. Here λ_{MRI} (see Eq. (1) in [96]) is the fastest-growing MRI wavelength and dx is the local grid spacing. The MRI can be properly captured if: (i) the quality factor $Q_{\mathrm{MRI}} \gtrsim 10$; and (ii) λ_{MRI} fits inside the remnant [97,98].

We compute the outgoing EM Poynting luminosity $L = -\int T_t^{r(\mathrm{EM})} \sqrt{-g} dS$ across spherical surfaces of coordinate radii between $r_{\mathrm{ext}} = 50\,M$ and $350\,M$. A summary of the above results is displayed in Table III. Note that we add an "P", "I" or "H" at the end of the tag name of a given configuration to denote the initial magnetic field configuration [i.e., P = magnetic field that extends from the stellar interior into the pulsarlike exterior, I = magnetic field confined in the stellar interior, or H = purely hydrodynamic (i.e., unmagnetized)].

III. RESULTS

The basic dynamics and final outcome of the NSNS models listed in Table III can be summarized in Fig. 1. Left and right columns display the evolution of the unmagnetized and magnetized representative cases at selected times, respectively. Gravitational radiation losses cause the orbital separation to shrink driving the binary merger (see second rows). Figure 2 displays the coordinate separation between NS centroids, defined as the coordinate position of the maximum value of the rest-mass density, for the magnetized cases. We note that the softer the EOS (see Sec. II B), the longer the inspiral phase. In particular, SLyM2.7P and Γ2M2.8P, binaries with the same initial rest-mass (see Table I) merge after ~ 6.2 and ~ 3.2 orbits, respectively, while H4M2.8P, the binary with the same ADM mass as the latter, merges after ~ 4.6 orbits. As shown in the left panel of Fig. 3, similar behavior is observed in the unmagnetized cases. This is anticipated because the seed magnetic field is initially unimportant dynamically (we recall that the initial magnetic pressure is only $\sim 0.3\%$ of P_{gas}) and hence cannot have a strong impact during the inspiral.

Following the merger, we note that:

(i) If the ADM mass of the binary is $\lesssim M^{\mathrm{thres}}$, then the merger outcome can be a short- medium- or long-lived HMNS that undergoes delayed collapse to a
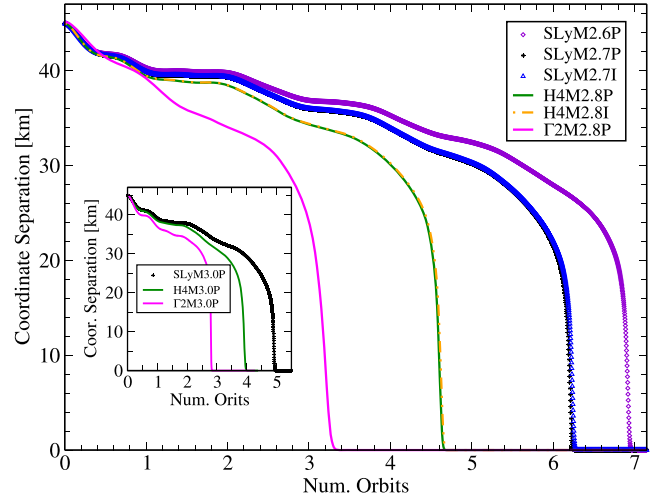

FIG. 2. Binary coordinate separation between NS centroids, defined as the position of the maximum value of the rest-mass density, for the magnetized cases displayed in Table III. The inset shows the binary separation for cases where the BH forms within the first ~ 3 ms following merger (i.e., prompt collapse and short-lived HMNS undergoing collapse).

BH immersed in an accretion disk (see second and third rows in Fig. 1). Although the masses of the NSNSs are slightly different (see Table I), there is an impact of the EOS on the lifetime of the transient: the softer the EOS, the shorter the HMNS lifetime τ_{HMNS}. In particular, the HMNS remnant in cases SLyM2.7P, H4M2.8P, and Γ2M2.8P lasts ~ 8.9 ms, ~ 9.3 ms, and ~ 17 ms, respectively (see Table III for other cases). In addition, the softer the EOS, the larger the amount of energy and angular momentum carried away by GWs. Note that the sensitivity of the HMNS lifetime to the magnetic field is physical and has been previously reported in [99]. However, as pointed out in [7], τ_{HMNS} depends on numerical resolution, even in unmagnetized simulations. High resolution studies may be required to accurately determine the HMNS lifetime.

Following the collapse of the HMNS, material with high angular momentum wraps around the BH, forming an accretion disk (see bottom panels in Fig. 1). If the accretion disk is magnetized then an incipient jet—i.e., a mildly relativistic outflow confined in a tightly wound, helical magnetic field [7]—is launched once the ratio $B^2/(8\pi\rho_0) \gtrsim 1$ above the BH poles. The incipient jet emerges regardless of the EOS or the initial magnetic field configuration (see Figs. 1 and 4 and middle panel in Fig. 5). These preliminary studies suggest that an incipient jet is the typical outcome of magnetized NSNS mergers.

We note that the jet launching time strongly depends on how close the total mass of the binary is to the threshold value for prompt collapse, which in
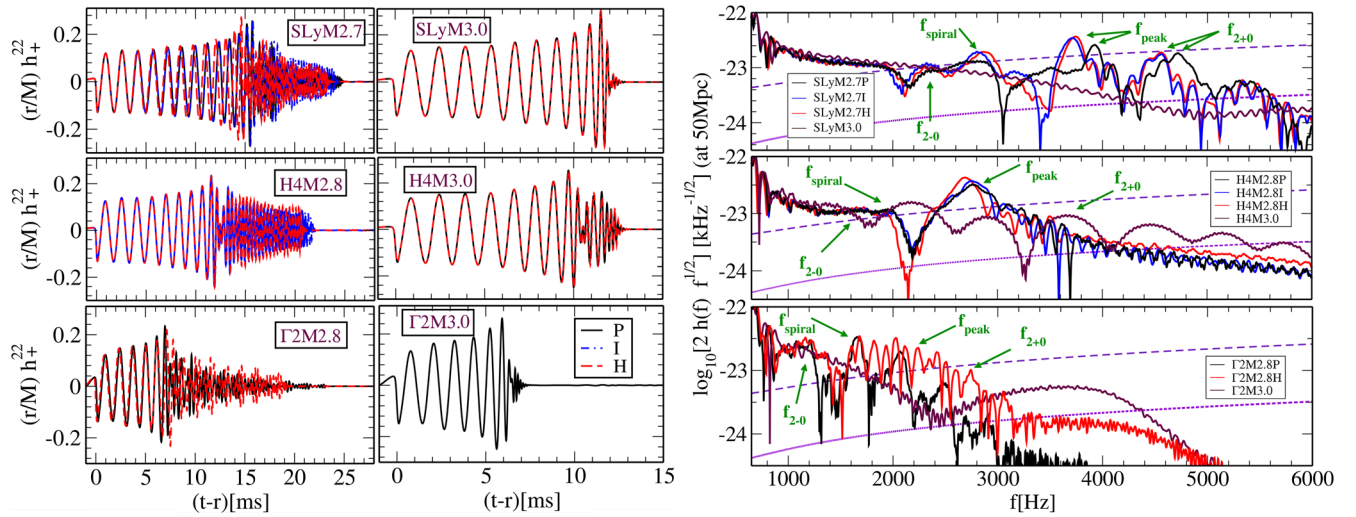
FIG. 3.   GW strain h_+^{22} (dominant mode) as functions of retarded time (left) at extracted coordinate radius $r_{ext} \approx 100~M$, and GW power spectrum of the dominant mode (right) at a source distance of 50 Mpc along with the aLIGO (dashed line) and Einstein Telescope (dotted line) noise curves of configurations in [58] for cases listed in Table III. Main spectral frequencies are denoted as $f_{2\pm0}$, f_{spiral}, and f_{peak} (see Table IV).
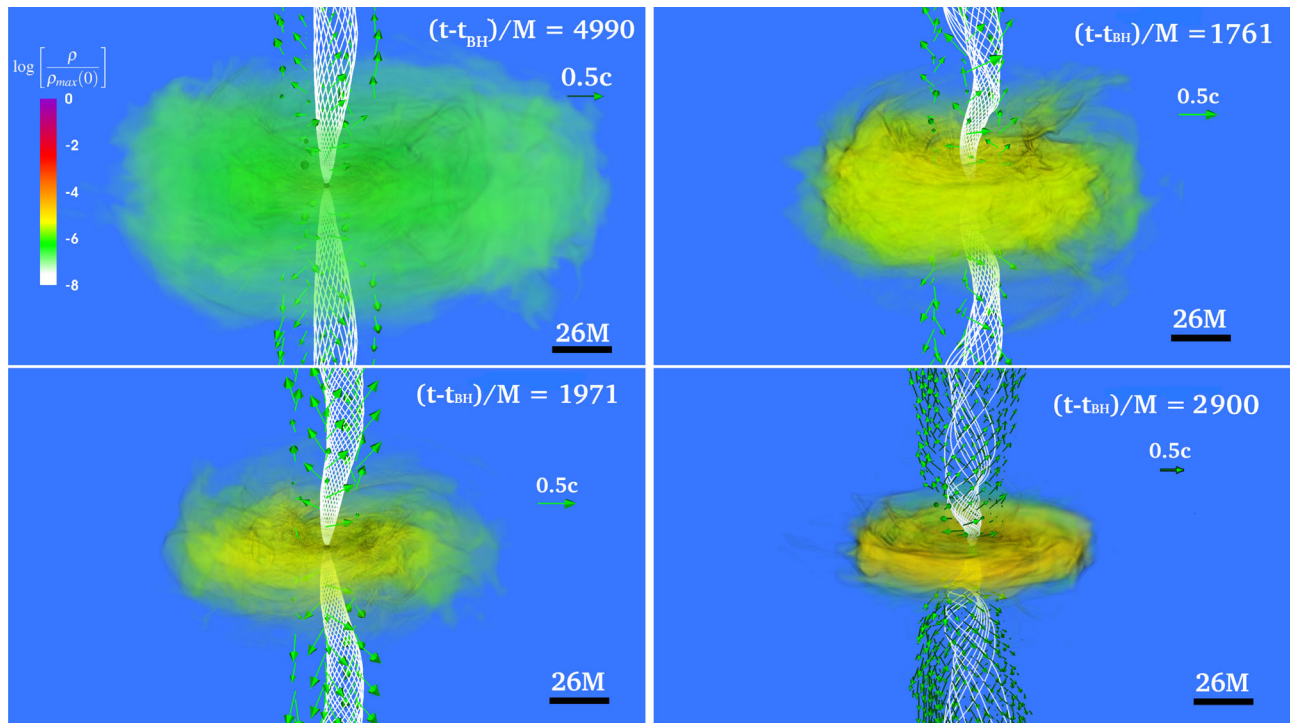

FIG. 4.   Volume rendering of the remnant BH + disk configuration for cases SLyM2.7I (top left), SLyM2.7P (top right), H4M2.8P (bottom left) and Γ2M2.8 (bottom right). The rest-mass density is normalized to the NS initial maximum value. White lines depict the magnetic field lines while the arrows display fluid velocities. The BH apparent horizon is displayed as a black surface. Here $M \sim 1.3 \times 10^{-2}$ ms ~ 4 km.

turn depends on the maximum mass configuration of a given EOS. For realistic EOSs, such as SLy or H4, the threshold mass for prompt collapse is ~ 1.3–$1.5~M_{sph} \simeq 2.82~M_\odot$ while for polytropic EOSs like $\Gamma = 2$ it is $\sim 1.7~M_{sph} \simeq 2.88~M_\odot$ [78,100–102]). The same values also apply to configurations with dynamically weak initial magnetic fields. In particular, we observe that in
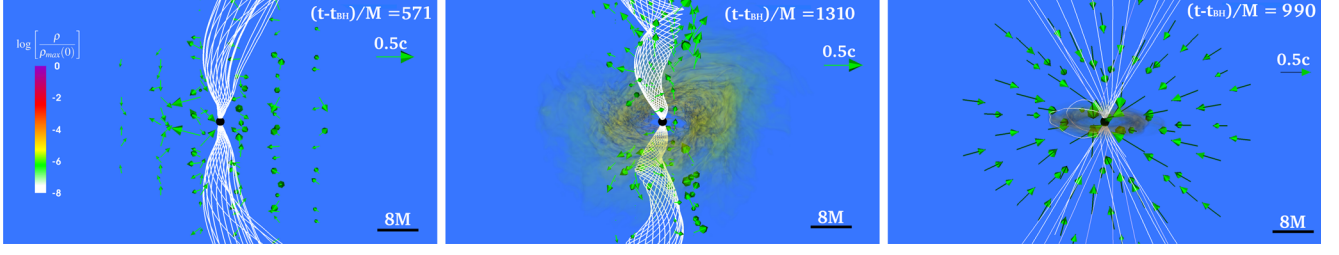
FIG. 5. Volume rendering of the remnant BH + disk configuration for cases SLyM3.0I (left), H4M3.0P (middle), and Γ2M3.1 (right). The rest-mass density is normalized to the NS initial maximum value. White lines depict the magnetic field lines while the arrows display fluid velocities. The BH apparent horizon is displayed as a black surface. Here $M \sim 1.5 \times 10^{-2}$ ms ~ 4.5 km.

SLyM2.7P a magnetically driven jet is launched after $t - t_{\mathrm{BH}} \sim 20$ ms while in SLyM2.7I it is launched after $\gtrsim 60$ ms (see below).

(ii) If the ADM mass of the binary is $> M^{\mathrm{thres}}$, then it undergoes prompt collapse to a BH surrounded by a small a disk with rest-mass of $\lesssim 0.5\%$ of the total rest-mass of the binary (see Fig. 5). Consistent with the results reported in [8], we do not observe a persistent outflow or tight magnetic field collimation in these cases (see left and right panels in Fig. 5).

We summarize below the outcome of our binary merger simulations during the HMNS and BH + disks phases of the evolution. We recall that our configurations differ in the EOS and seed magnetic field (magnitude and initial geometry). Key results from these simulations are displayed in Table III.

A. Delayed collapse

Figure 6 shows the evolution of the magnetic energy for all cases in Table III. During the inspiral the magnetic energy $\mathcal{M}$ either decreases or at most is slightly amplified until merger. This behavior depends on the NS compactness and the initial seed magnetic field geometry. In our extreme cases (see Table I), we observe that at merger $\mathcal{M}$ has decreased by a factor of ~ 1.5 in SLyM2.6P, while in Γ2M2.8P it has been amplified by roughly the same factor. Our simulations show that until merger, the frozen-in magnetic field lines, which are anchored to the fluid elements, are simply advected (see second row, right panel in Fig. 1). Neither spurious magnetic fields or appreciable changes in the internal structure of the stars are observed. The relative changes in the central NS rest-mass density during inspiral is $\lesssim 0.2\%$. It has been suggested that pure poloidal magnetic field configurations are unstable on an Alfvén timescale (see e.g., [103,104]). In our models, the Alfvén timescale can be estimated as (see Eq. (2) in [105])

$$\tau_{\mathrm{Alfven}} \sim \frac{R}{v_A} = \frac{\sqrt{4\pi\rho_0}R}{|B|} \sim 10|B|_{15}^{-1}R_{10}\rho_{0,14}^2 \text{ ms}, \quad (6)$$

where $|B|_{15} = |B|/(10^{15}\,\mathrm{G})$, $R_{10} = R/(10\,\mathrm{km})$ and $\rho_{0,14} = \rho_0/(10^{14}\,\mathrm{g/cm^3})$ are the characteristic strength of the magnetic field, the radius, and rest-mass of the NS, respectively. In all our cases, we find that the central Alfvén time is $\tau_{\mathrm{Alfven}} \lesssim 7.5$ ms, and hence their inspiral phase last at least one Alfvén time (see Table III). In addition to magnetic instabilities, tidal effects, which can drive fluid motion in the stars, may also change the magnetic energy [26]. We are currently investigating this effect.

During the next ~ 3 ms following merger, the magnetic energy is exponentially amplified due mainly to the KH instability. Such an effect has been found in high resolution studies reported in [82,83]. We note that in binaries endowed with a pulsarlike interior + exterior magnetic field, $\mathcal{M}$ is amplified by a factor of ~ 20 (see Fig. 6). In contrast, $\mathcal{M}$ is only amplified by a factor ~ 10 in those endowed with a magnetic field confined to the NS. Further amplification during the HMNS phase is only
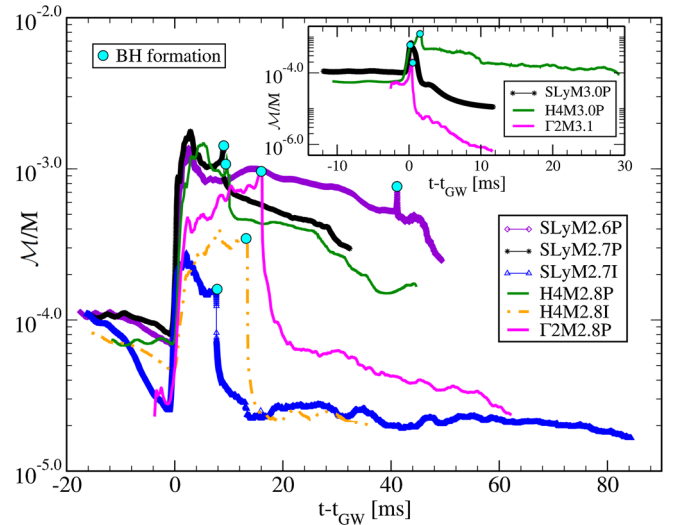

FIG. 6. Total magnetic energy $\mathcal{M}$ normalized by the corresponding ADM mass ($M \sim 5. \times 10^{54}$ erg) versus coordinate time for cases listed in Table III. The inset displays the short-lived HMNS and prompt collapse cases. Dots mark the BH formation time t_{BH}; t_{GW} is the merger time.

observed in Γ2M2.8P. In all other cases, $\mathcal{M}$ slightly decreases.

Top panels in Fig. 7 display the contours of the λ_{MRI}-quality factor Q_{MRI} on the equatorial plane for SLyM2.7P (left) and SLyM2.7I (right) after the transient HMNS has settled down ($t - t_{\mathrm{GW}} \sim 5$ ms). This parameter must be $\gtrsim 10$ in order to resolve MRI. We note that $Q_{\mathrm{MRI}} \gtrsim 10$ over a rather lager portion of the HMNS remnant (central core + cloud of matter that has wrapped around it) of SLyM2.7P. By contrast, Q_{MRI} is larger than 10 only in the bulk of the central core of the HMNS of SLyM2.7I, and by at most 4 in the external cloud of matter (low-density regions). Bottom panels in Fig. 7 show the rest-mass density of the HMNS on the meridional plane overlaid by λ_{MRI} along the x coordinate. For the MRI to be unstable at a given position, the HMNS must extend to a local height above λ_{MRI}. In the above cases, λ_{MRI} fits within a region where the rest-mass density is $\gtrsim 10^{11.3}$ g/cm^3, well above of the floor density. Based on the above results, we conclude that MRI can operate all over the transient remnant in SLyM2.7P, but

only in the central core of the HMNS of SLyM2.7I. This is expected because right after merger, a double-core structure is formed by the two central cores of the merging NS. These two cores collide and bounce repeatedly until they eventually merge, forming a single central core. During this process, the external layers of the merging stars gain angular momentum due to orbital angular momentum advection and to torques arising from the nonaxisymmetric structure of the double-core, as well as to magnetic instabilities (MRI and magnetic winding). This causes the external layers to expand and simultaneously the central core to shrink, forming a massive central core immersed in a low density cloud. In the HMNS remnant of SLyM2.7I, the cloud of matter is formed by low-magnetized material. We recall that in this case, the magnetic field is initially confined within interior regions with pressure larger than 1% of the initial maximum pressure of the NS (see Sec. II B), and hence its outermost layers are initially unmagnetized. Consistent with this, once the central core of the HMNS collapses, the magnetic energy in SLyM2.7I
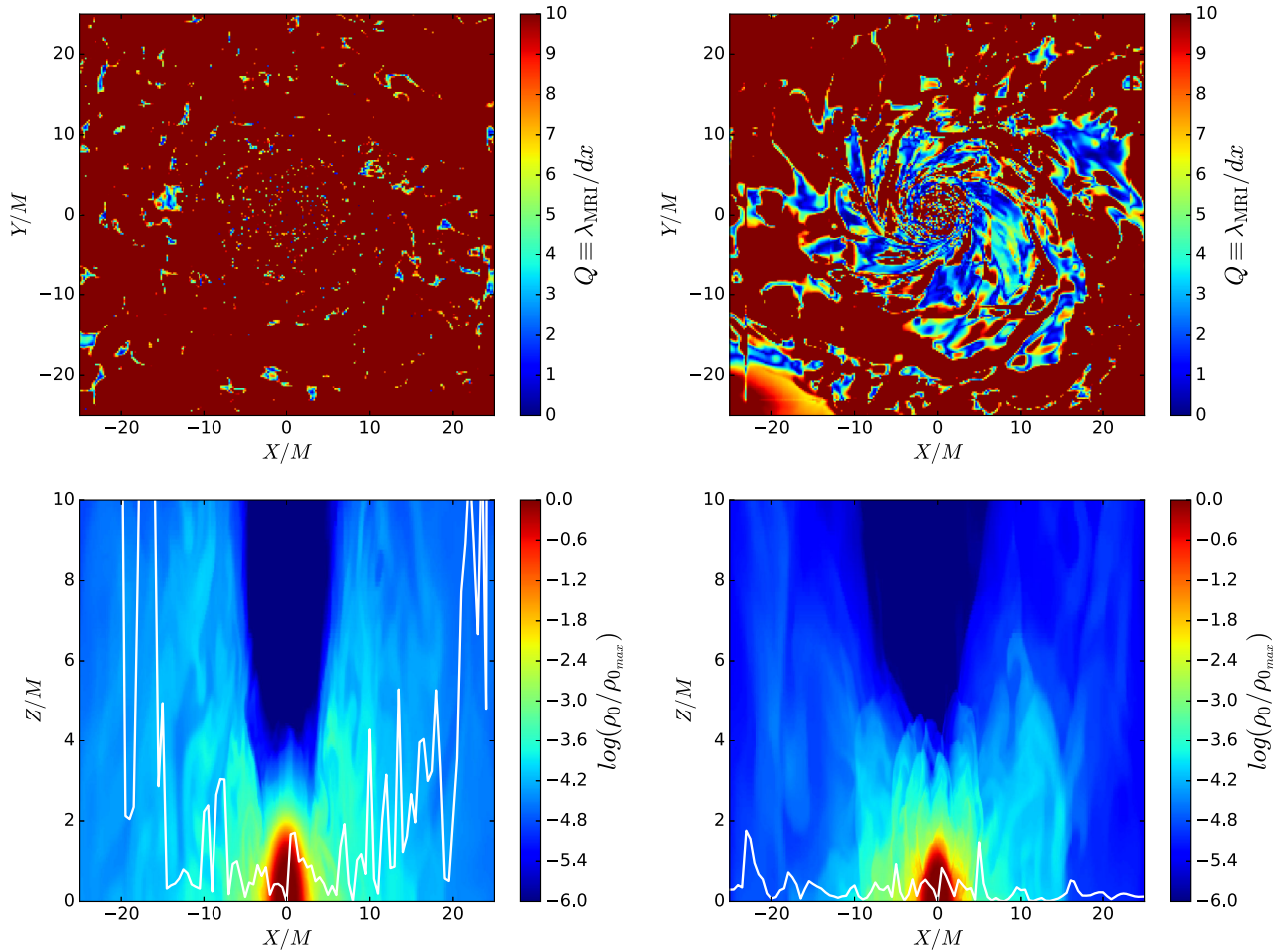

FIG. 7.   Contours of the quality factor $Q = \lambda_{\mathrm{MRI}}/dx$ on the equatorial plane (top), and the rest-mass density of the transient HMNS normalized to its initial maximum value (log scale) along with λ_{MRI} (white line) on the meridional plane (bottom), at $t - t_{\mathrm{GW}} \sim 5.2$ ms for SLyM2.7P (left) and SLy2.7I (right). Similar behavior is observed in all other cases in Table III.

decreases and settles into a steady state faster than in SLyM2.7P (see Fig. 6). Similar behavior is observed in all cases in Table III; MRI is operating all over the HMNS formed after the merger of an NSNS initially seeded with a pulsar-like interior + exterior magnetic field, and is only operating in the central core of the HMNS of those binaries seeded with a magnetic field confined inside the star. Such behavior has been reported before (see e.g Fig. 17 in [48]). Notice that very high-resolutions are required to properly capture MRI in the low density regions of the HMNS formed after the collapse of stars initially endowed with magnetic field confined to their interior.

Calculating the effective ShakuraSunyaev $\alpha_{\rm SS}$ parameter in the HMNS, we find that $\alpha_{\rm SS}$ ranges between $\sim 10^{-3.5}$ to $\sim 10^{-2}$ (see Table III). Similar values were reported in previous, high-resolution NSNS merger studies [106]. Therefore, we expect that magnetic turbulence, which grows on an effective viscous timescale $\tau_{\rm vis} \sim R_{\rm HMNS}^{3/2} M_{\rm HMNS}^{-1/2} \alpha_{\rm SS}^{-1} \sim 1\text{--}10$ ms (see Eq. 3 in [105]) where $R_{\rm HMNS}^{3/2}$ and $M_{\rm HMNS}$ are the characteristic radius and mass of the HMNS, is also operating in the remnant. We confirm this on meridional slices of the transient star, where we see evidence for turbulent magnetic fields. Magnetic turbulence strongly depends on resolution. The results in [106] show that numerical (diffusion) artifacts can suppress a sustained magnetic turbulence, hence values of $\alpha_{\rm SS}$ quoted in Table III may be underestimated. Higher resolutions studies may shorten the viscous timescale $\tau_{\rm vis}$.

Following merger, nonaxisymmetric oscillation modes of the HMNS, which persist until stellar collapse to a BH,

trigger the emission of quasiperiodic GWs (see Fig. 3). The dissipation of angular momentum due to GW radiation is more efficient in the unmagnetized cases. In particular, we find that in SLy2.6H around 17% of the total angular momentum is carried away by gravitational radiation, while in SLy2.6P it is around 14% (see Table III for other cases). However, centrifugal support due to differential rotation allows the HMNS remnant of SLy2.6H to survive for more than ~ 43 ms after merger, time at which we terminate its evolution. By contrast, magnetic turbulence in the HMNS remnant damps the centrifugal support, driving the collapse to a BH roughly at ~ 41 ms following merger. This effect is shown in Fig. 8 in which the averaged angular rotation profiles of the HMNSs for SLyM2.7 and H4M2.8 are plotted at regular times (in multiples of the initial central period of the HMNS). In contrast to the unmagnetized cases (see insets in Fig. 8) where the angular velocities roughly maintain their initial profiles, in the magnetized cases the central core of the HMNS becomes almost uniformly rotating over an Alfvén timescale (see Eq. (6), while its external, low density envelope maintains a Keplerian rotation profile. These results demonstrate that angular momentum redistribution from the inner to the outer regions due to nonaxisymmetric torques and GW losses are inefficient mechanisms compared to magnetic fields in removing the added centrifugal support provided by differential rotation [105].

Angular momentum redistribution eventually triggers HMNS collapse to a highly spinning BH immersed in an accretion disk (see bottom panels in Fig. 1). The stiffer the EOS, the heavier the BH remnant and the higher its spin
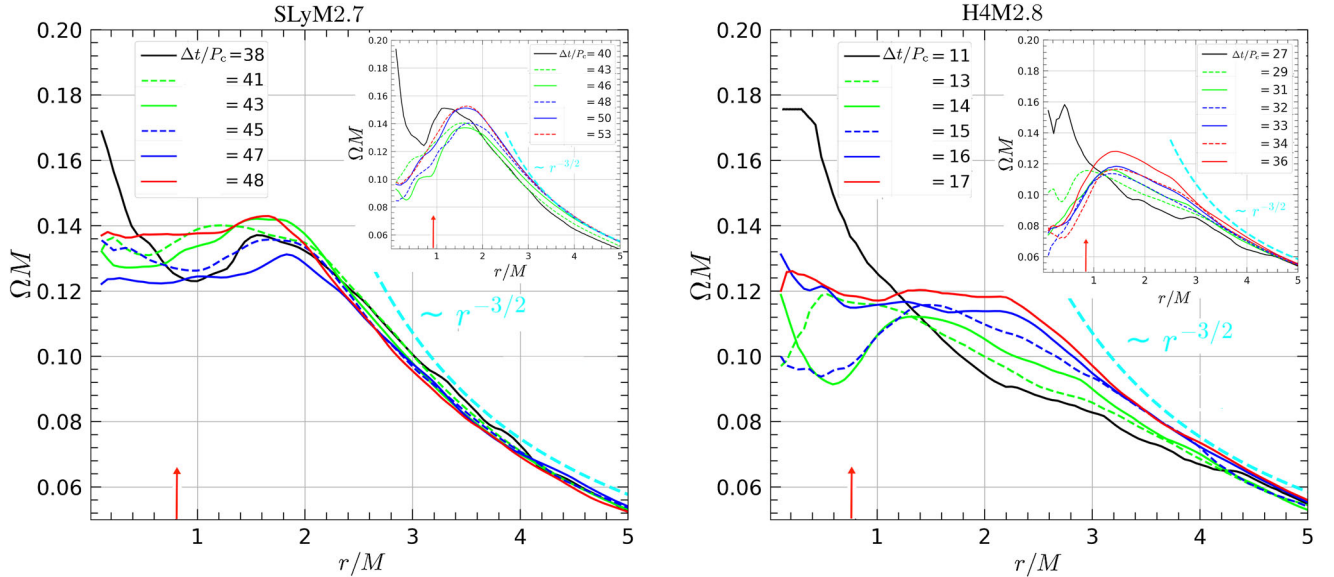

FIG. 8. Average rotation profile of the HMNS (see Eq. (2) in [47]) for magnetized cases SLyM2.7P (left) and H4M2.8P (right) in the equatorial plane at $\Delta t = t - t_{\rm HMNS}$, together with a Keplerian angular velocity profile. The inset displays the corresponding unmagnetized cases (see Table III). The arrow marks the coordinate radius containing $\sim 50\%$ of the total rest-mass of the transient remnant. Here $t_{\rm HMNS}$ is the HMNS formation time, with P_c the central HMNS period at $t = t_{\rm HMNS}$, which is $P_c \sim 0.25$ ms and $P_c \sim 0.51$ ms for SLy and H4 cases, respectively.

parameter. In particular, the mass and spin of the BH remnant in SLyM2.7P are ~2.45 $M_\odot$ and $a/M_{BH} \sim 0.62$, respectively, while in Γ2M2.8P they are ~2.65 $M_\odot$ and $a/M_{BH} \sim 0.74$ (see Table III for other cases). As mentioned before, after merger angular momentum is transferred from the inner to the outer layers of the stars, causing the latter to expand. In the soft EOS (SLy) a significant fraction of the matter from the outer layers of the star gains enough angular momentum to expand and remain outside the ISCO once the bulk of the star collapses. Eventually this material wraps around the BH forming the accretion disk. In the stiff EOS (Γ = 2), the external layers remain closer to the bulk of the star and, hence, when the BH forms, most of them get caught inside the ISCO and eventually are swallowed by the BH, leaving less material to form the accretion disk. Consistent with this, Fig. 9 shows the rest-mass of the accretion disk for all cases in Table III, which ranges between 3% in Γ2M2.8P (stiff EOS) to 7% in SLyM2.7P (soft EOS) of the total mass of the system.

In our long-lived HMNS (SLy2.6P) case, in which the transient remnant has a lifetime of ~41 ms, angular momentum transfer operates for many rotation periods, and hence more material from the external layers can be released in the surroundings of the central core, forming a puffy disk that wraps around it. Consistent with this, Fig. 9 demonstrates that the accretion disk of the SLy2.6P remnant is the most massive one of our cases, and hence it has the lightest BH (~2.26 $M_\odot$) with the lowest dimensionless spin ($a/M_{BH} \sim 0.47$).

Right before the collapse of the HMNS, the rms magnetic field strength ranges between ~$10^{15.8}$ and $10^{16.2}$ G (see Table III), consistent with the values reported in [82,83]. Shortly after BH formation, the inner region of the star, which contains most of the magnetic energy, is promptly swallowed by the BH, causing the magnetic energy to drop quickly in $\Delta t \lesssim 3$ ms and then slightly decrease thereafter as the accretion proceeds (see Fig. 6). During the BH + disk evolution phase we do not find evidence of magnetic field enhancement. In all cases, the rms value of the magnetic field in the bulk of the disk remnant is $\lesssim 10^{15}$ G.

Shortly after BH formation, material ejected during merger and HMNS formation begins to fall back, increasing the ram-pressure. This pressure is so strong that it prevents the launching of a wind [107]. However, as shown in the third row and right panel in Fig. 1, magnetic winding has begun even before BH formation. As the accretion proceeds (see Fig. 10), the baryon-loaded environment in the polar region above the BH gradually becomes thinner until the ratio $B^2/(8\pi\rho_0)$ exceeds unity. At this point, the inflow halts and eventually a magnetically supported outflow is triggered—the incipient jet.

1. Magnetic field initially confined inside the star

During the HMNS phase, the enhancement of the magnetic energy in case H4M2.8I is a factor of ~2 larger than that in SLyM2.7I (see Fig. 6). However, following BH formation, we note that in both cases $\mathcal{M}$ plummets and settles into a steady state. By $t - t_{BH} \sim 3$ ms the magnetic energy in both cases is $\mathcal{M}/M \sim 10^{-4.6}$ and roughly remains constant until the termination of our simulations. We evolve these two cases during the next $t - t_{GW} \sim 20$ ms and, consistent with the results reported in [28], we observe a persistent inflow toward the BH and an intermittent and weak helical magnetic field structure above the BH poles ($B_p \sim 10^{15.8}$ G), though in both cases we note that the ratio $B^2/(8\pi\rho_0)$ is slightly rising as the accretion takes place. As the behavior of the BH + disk remnant in these two cases is basically the same, given our finite computational
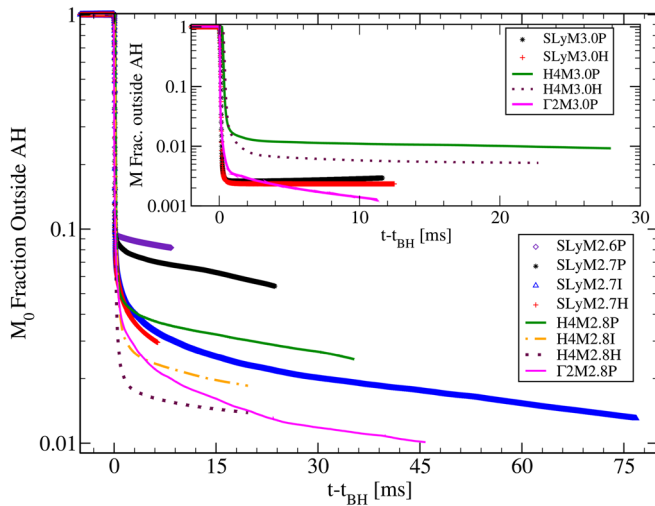

FIG. 9. Rest-mass fraction outside the BH apparent horizon versus coordinate time for all cases listed in Table III.
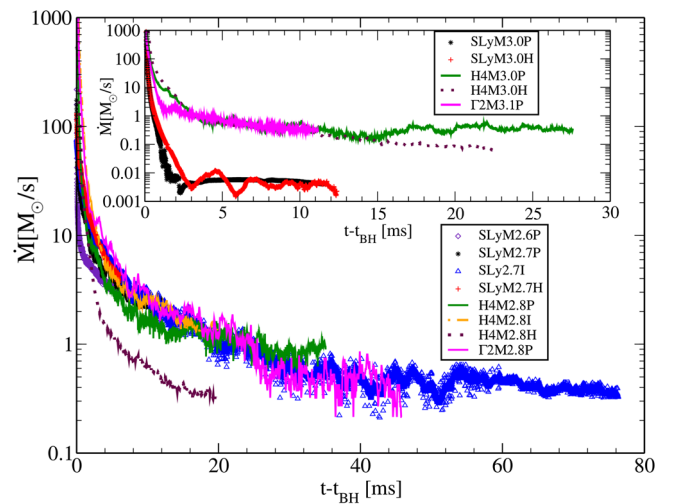

FIG. 10. Rest-mass accretion rate for all cases listed in Table III computed via Eq. (A11) in [93].

resources we chose to continue only the evolution of SLyM2.7I. This case has the longest accretion disk lifetime (see Table III), consistent with the sGRB engine lifetime [49–52].

By $t - t_{BH} \sim 3000\ M \sim 40$ ms, the magnetic pressure in the regions immediately above the BH remnant is high enough to balance the ram pressure of the fall-back material and hence the inflow halts. Fluid velocities then begin to turn around and magnetically dominated regions (i.e., $B^2/(8\pi\rho_0) \gtrsim 1$) gradually expand. As these regions expand, the field lines tighten around them forming a helical structure, inside of which fluid elements escape. By $t - t_{BH} \sim 4200\ M \sim 56$ ms the outflow, which has been accelerated to Lorentz factor $\Gamma_L \lesssim 1.25$, reaches a height of $\sim 100\ M \sim 400$ km, and so an incipient jet has formed (see top left panel in Fig. 4). Following [7], we define the half-funnel opening angle θ_f as the boundary of the region above the BH in which $B^2/(8\pi\rho_0) \gtrsim 10^{-2}$. In this case, we find that the half-opening angle is $\theta_f \sim 25°$.

We also assess if the BZ mechanism is operating in the BH + disk remnant, as we found in our previous studies. For this, we compare the outgoing Poynting luminosity L_{EM} generated in our simulations (see Sec. II D) with the EM power generated by the BZ mechanism given in [108]

$$L_{BZ} \sim 10^{52} \left(\frac{\tilde{a}}{0.75}\right)^2 \left(\frac{M_{BH}}{2.8\ M_\odot}\right)^2 |B_p|_{16}^2\ \text{erg/s} \quad (7)$$

where $|B_p|_{16} \equiv |B_p|/10^{16}$ G is the strength of the magnetic field at the BH poles. The Poynting luminosity, time-averaged over the last ~ 5 ms before the termination of our simulation for SLyM2.7I, is $10^{51.3}$ erg/s (see Fig. 11). On the other hand, $|B_p| \sim 10^{15.8}$ G, and $L_{BZ} \sim 10^{51.4}$ erg/s, in close agreement.
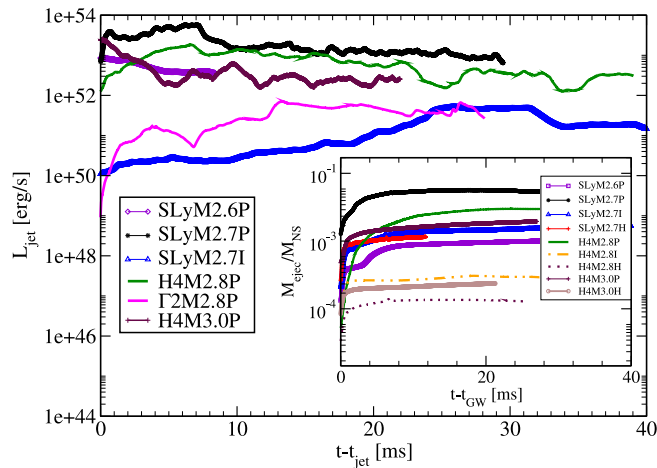

FIG. 11. Outgoing EM (Poynting) luminosity following jet launching at a coordinate sphere of radius $r = 160\ M$ for cases listed in Table III. The inset shows the rest-mass fraction of escaping matter following the GW peak amplitude (merger).

Another key feature of the BZ mechanism is that the field lines rotate at frequency $\Omega_F \approx 0.5\Omega_H$ for $\tilde{a} \ll 1$ if the field has a monopole geometry and its surroundings are strongly forcefree ($B^2/(8\pi\rho_0) \gg 1$) [39]. Here Ω_H is the angular frequency of the BH. The numerical results in [109] showed that for a monopole magnetic field around a spinning BH, the field lines at the BH poles rotate at a frequency of $\sim 0.5\Omega_H$ for a BH spin $\tilde{a} = 0.1$, and between $\sim 0.52\Omega_H$, at the BH pole, and $\sim 0.49\Omega_H$, near the equator, for a BH spin $\tilde{a} = 0.9$. Following [9], we measure Ω_F on a meridional plane passing through the BH centroid and along coordinate semicircles of radii r_{BH} and $2r_{BH}$ within the magnetically dominated (or mildly forcefree) region. We find that the field lines differentially rotate with a frequency in the range $\Omega_F/\Omega_H \sim 0.2$–$0.6$. As pointed out in [9,110] the differences from the expected $\Omega_F/\Omega_H \sim 0.5$ BZ-factor may be due to artifacts such as the deviation from strictly forcefree conditions, deviations from monopole geometry and/or lack of resolution. Our cumulative results nevertheless suggest that the BZ mechanism is operating in our system, as concluded in [7,47].

2. Pulsarlike magnetic field

The magnetic energy exponentially increases during merger and slightly changes during the HMNS phase. As shown in Fig. 6, by $t - t_{GW} \sim 1.5$ the magnetic energy in all these cases is amplified roughly by the same factor, which is $\gtrsim 3$ times larger than in those seeded with a magnetic field confined inside the star. We note that in HMNS cases with intermediate lifetime, the decrease of the magnetic energy following BH formation depends on the EOS. The stiffer the EOS, the faster $\mathcal{M}$ decreases. In particular, the magnetic energy in SLyM2.7P decreases by a factor of ~ 2 in $t - t_{BH} \sim 3$ ms, while in $\Gamma 2M2.8P$ it decreases by a factor of ~ 10 during the same period of time. As shown in Fig. 6, at the termination time of our simulations, the BH + disk remnants of the SLy and H4 cases have a larger magnetic energy than that in $\Gamma 2M2.8P$. This is likely due to the amount of magnetized material that wraps around the BH forming the accretion disk. As mentioned before, Fig. 9 shows that the stiffer the EOS, the smaller the accretion disk, so less magnetized material outside of the BH.

Consistent with our previous results [7], as the magnetic field is not amplified during the BH + disk phase, a magnetically driven jet is launched only after the density in the polar region above the BH poles decreases to values $\rho_0 \lesssim B^2/8\pi$. Figures 1 (right bottom panel), 4 and 5 (middle panel) show the helical structure of the magnetic field once the incipient jet has reached steady state. There is a trend in the jet launching time: the shorter the HMNS lifetime, the faster the emergence of the incipient jet. In particular, the HMNS lifetime in H4M3.0P is $\tau_{HMNS} \sim 2.5$ ms and the system launches an incipient jet at time $t - t_{BH} \sim 19$ ms following BH formation.

By contrast, the HMNS lifetime in H4M2.8P is $\tau_{HMNS} \sim$ 9.6 ms and its BH + disk remnant launches a jet by $t - t_{BH} \sim 27$ ms following BH formation. Similarly, $\tau_{HMNS} \sim 17$ ms in Γ2M2.8P and the jet is launched by $t - t_{BH} \sim 40$ ms. This time difference is likely due to the ram-pressure of the falling-back debris toward the BH. The shorter the HMNS lifetime, the less angular momentum deposited in the outer layers of the transient remnant, and so the less material released in the atmosphere. This effect is translated in lighter baryon-loaded environments, which allows the ratio $B^2/(8\pi\rho_0)$ to grow to values $\gtrsim 1$ more rapidly. Consistent with this, the BH + disk remnant of SLyM2.7P launches an incipient jet by $t - t_{BH} \sim 24$ ms, while that in SLyM2.6P (the case with the longest τ_{HMNS}) launches it by $t - t_{BH} \sim 26$ ms. In the latter case angular momentum transfer processes operate for longer times than in the former. This behavior is confirmed in Fig. 12, which displays the force-free parameter $B^2/(8\pi\rho_0)$ once the incipient jet is well-developed for SLyM2.7P (left), H4M2.8P (middle), and Γ2M2.8P (right). The shorter the τ_{HMNS}, which results in lighter baryon-loaded environments, the higher the above ratio.

In all cases, magnetically dominated regions ($B^2/(8\pi\rho_0) \gtrsim 1$) extend to heights $\gtrsim 20 \, M \approx 20r_{BH}$ above the BH, where r_{BH} is the BH apparent horizon radius. As before, we use the $B^2/(8\pi\rho_0) \sim 10^{-2}$ contour as the definition of the funnel boundary, which has an opening half-angle of $25°$–$35°$. We note that in the funnel the maximum value of the Lorentz factor is $\Gamma_L \sim 1.2$–1.25 (see Table III) and hence the outflow is only mildly relativistic. However, as pointed out in [111], the maximum attainable Lorentz factor of a magnetically-powered, axisymmetric jet is $\Gamma_L \approx B^2/(8\pi\rho_0)$. Therefore, we expect that the fluid elements inside the funnel can be accelerated to values $\Gamma_L \gtrsim 100$ as required by most sGRB models [37].

Figure 11 displays the outgoing Poynting luminosity L_{EM}. We find that $L_{EM} \sim 10^{51.3}$–$10^{52.8}$ (see Table III). These values reside in the narrow band of luminosities shown theoretically in [112] to constitute a "universal range" for most BH + disk + jet systems arising from compact binary mergers containing NSs, as well as from

the magnetorotational collapse of massive stars. This band also agrees with the narrow range characterizing the observed luminosity distributions of over 400 short and long GRBs with distances inferred from spectroscopic redshifts or host galaxies [113] (see also [49]). A similar universal range applies to the BH accretion rates upon jet launching, also shown in [112], and the range shown in Fig. 10, is also consistent with this expectation. We also note that near the end of the simulations, the magnetic field magnitude above the BH pole is $\sim 10^{15.8}$–$10^{16.2}$ G and hence using Eq. (7) we have $L_{BZ} \sim 10^{51.4}$–$10^{52.1}$, which is roughly consistent with our numerical results as well. As before, we compute the angular frequency of the magnetic field lines on a meridional plane passing through the BH centroid and along coordinate semicircles of radii r_{BH} and $2r_{BH}$ within the force-free region. In all these cases the field lines differentially rotate with a frequency in the range $\Omega_F \sim 0.1$–0.54, and according to our previous discussion, it is likely that the BZ mechanism is operating in our systems.

B. Prompt collapse

The basic dynamics of NSNSs undergoing prompt collapse has been reported in [8], where it was found that, shortly after the stars touch for the first time the remnant undergoes collapse to a BH. As there is no angular momentum transport due magnetic instabilities, only the external and low density outer layers of the stars, which are able to gain enough angular momentum due to tidal torques, are pushed away from the bulk of the merging stars. Eventually, this material wraps around a highly spinning BH, forming an accretion disk with a rest-mass $\lesssim 0.5\%$ of the total rest-mass of the system (see Table III). The rest-mass of the BH remnant settles to $M_{BH} \gtrsim 2.8 \, M_\odot$, with a dimensionless spin parameter $a_{BH}/M_{BH} \sim 0.8$. The BH remnant in prompt collapse cases is the heaviest and with the highest spin of all our cases. These results are anticipated because basically all the material is swallowed by the nascent BH.

Consistent with the previous results, the inset in Fig. 6 shows that during the merger the magnetic energy is continuously amplified until BH formation, when it
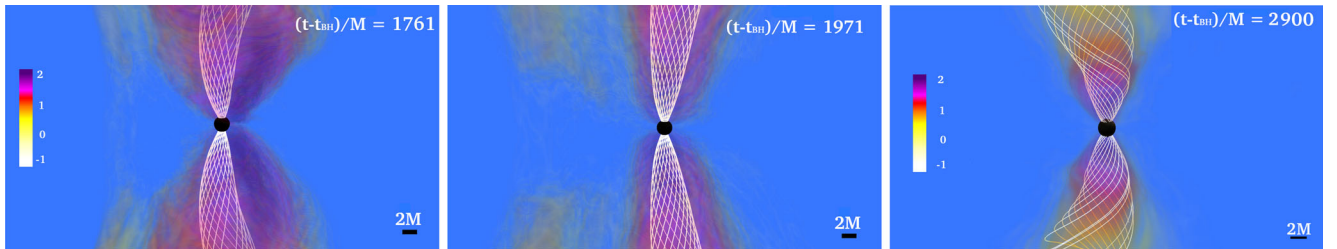

FIG. 12. Volume rendering of the forcefree parameter $B^2/(8\pi\rho_0)$ (log scale) after the incipient jet is well-developed for case SLyM2.7P (left), H4M2.8P (middle), and Γ2M2.8P (right). Magnetic field lines (white lines) are plotted inside regions where this ratio is $\gtrsim 10^{-2}$ (funnel boundary). Magnetically dominated regions ($B^2/(8\pi\rho_0) \gtrsim 1$) extend to heights $\gtrsim 20 \, M \sim 20r_{BH}$ above the BH (black sphere). Here $M \sim 1.3 \times 10^{-2}$ ms ~ 4 km.

then plummets. By $t - t_{\mathrm{BH}} \sim 2$ ms it falls to values $\mathcal{M}/M \lesssim 10^{10^{-5}}$ and continuously decreases thereafter. We track the evolution of the BH + disk remnant for $t - t_{\mathrm{BH}} \sim 15$ ms. We note that on x-z meridional slices passing through the BH centroid, regions with $B^2/(8\pi\rho_0) \sim 10^{-0.6}$ begin to expand as material in the polar region is accreted. By $t - t_{\mathrm{BH}} \sim 9$ ms, these regions reach a height of $\sim 10 r_{\mathrm{BH}}$, where the magnetic pressure is high enough to balance the ram pressure of the fall-back material. Subsequently, we observe that these regions expand and contract until the termination of our simulations. As shown in the left and right panels of Fig. 5, we do not find evidence of an outflow or magnetic field collimation, hence no jet.

C. Dynamical ejection of matter

The inset of Fig. 11 shows the fraction of the dynamical ejection of matter (ejecta) following the GW peak amplitude for all cases in Table III. These values are roughly consistent with those reported previously (see e.g., [89,90]).

We note that the EOS and the seed magnetic field (geometry and strength) have a strong impact on the ejecta. The softer the EOS, the larger the amount of matter ejected following the NSNS merger. In particular, the ejecta in SLyM2.7P is a factor of ~ 3 larger than that in H42.8P. This result is anticipated because, as mentioned above, a compact object modeled by a soft EOS cannot hold high angular momentum material. During merger, orbital angular momentum transfer by tidal torques induces the ejection of the outer layers of the stars. A significant fraction of this material gains enough energy to escape. The ejecta in SLy2.7I (configuration with a poloidal magnetic field confined in the NS) and SLy2.7H (unmagnetized configuration) is a factor of ~ 5 and ~ 8 smaller than in SLy2.7P, respectively (see Table III for other cases). It has been suggested that the magnetic field lines of a rotating compact object may accelerate fluid elements due to a magnetocentrifugal mechanism [53]. These results collectively suggest that GRMHD studies are required to fully understand kilonova signals from GW170817-like events.

Ejecta masses $\gtrsim 10^{-3}\ M_\odot$ are expected to lead to detectable, transient kilonova signatures (see e.g., [114]) powered by radioactive decay of unstable elements formed by the neutron-rich material ejected during NSNS mergers [114,115]. An analytical model that computes the peak rise times, bolometric luminosities and the effective temperatures for kilonovae was derived in [54]. This model assumes an ejecta of mass M_{esc} that is spherically distributed and expanding homologously with an average speed $\langle v_{\mathrm{esc}}\rangle$ and characterized by a gray opacity κ_γ. The peak time of the kilonova emission τ_{peak} can be then estimated as [54]

$$\tau_{\mathrm{peak}} \sim \sqrt{\frac{M_{\mathrm{esc}}\kappa_\gamma}{4\pi\langle v_{\mathrm{esc}}\rangle c}}$$

$$\approx 4.6\ \mathrm{days}\left(\frac{M_{\mathrm{eje}}}{10^{-2}M_\odot}\right)^{-1/2}\left(\frac{\langle v_{\mathrm{eje}}\rangle}{0.1\ c}\right)^{-1/2}, \quad (8)$$

assuming a gray opacity of $\kappa_\gamma = 10\ \mathrm{cm}^2/\mathrm{g}$. This opacity corresponds to ejecta containing a significant fraction of lanthanides and actinides (i.e., ejecta with an initial electron fraction $Y_e \lesssim 0.25$) [116,117]. The peak luminosity of the ejecta can be approximated by

$$L_{\mathrm{knova}} \sim 2.4 \times 10^{40}\left(\frac{M_{\mathrm{eje}}}{0.01\ M_\odot}\right)^{0.35}\left(\frac{\langle v_{\mathrm{eje}}\rangle}{0.1\ c}\right)^{0.65}\ \mathrm{erg/s} \quad (9)$$

Finally, assuming black body emission, and using the Stefan-Boltzmann law, the effective temperature at the peak can be estimated as [54]

$$T_{\mathrm{peak}} \sim 2.15 \times 10^3\left(\frac{M_{\mathrm{eje}}}{0.01\ M_\odot}\right)^{-0.16}\left(\frac{\langle v_{\mathrm{eje}}\rangle}{0.1\ c}\right)^{-0.09}\ \mathrm{K} \quad (10)$$

Using the above formulas, we estimate that the bolometric luminosity of potential kilonovae signals is $L_{\mathrm{knova}} = 10^{40.6\pm0.5}$ erg/s with rise times of $\tau_{\mathrm{peak}} \sim 0.4$–5.1 days and an effective temperature $T_{\mathrm{peak}} \sim 10^{3.5}$ K (see Table III). This temperature can be translated into a peak wavelength $\lambda_{\mathrm{peak}} = 1.35 \times 10^3\ \mathrm{nm}(T_{\mathrm{peak}}/10^{3.33}\ \mathrm{K})^{-1}$ [54]. We found that $\lambda_{\mathrm{peak}} \sim 730$–1830 nm, and the emission can be detected with current or planned telescopes, such as ALMA or the Vera C. Rubin observatory [55,56].

D. Gravitational wave signals

The left panel of Fig. 3 shows the GW strain of the dominant (2,2) mode as a function of retarded time for cases in Table III. We note that the amplitude differences between the unmagnetized and magnetized cases are less than 3% and their GW peaks occur roughly at the same time. The largest difference between the GW peak (merger) times of the unmagnetized and magnetized SLyM2.7 binaries is $\sim 83\ M \sim 1.1$ ms. These results confirm that the seed magnetic field used here does not significantly impact the global dynamics during inspiral.

Following merger, the GW strain either comes to an abrupt end following the quasinormal ringdown modes of the BH, in prompt collapse cases, or decays as the (initially nonaxisymmetric) HMNS remnant settles prior to its collapse. During this period, the waveform amplitudes in SLyM2.7 and Γ2M2.8 are roughly the same, and diminish faster than those in H4M2.8.

To assess the impact of the magnetic field during the postmerger phase on the GW forms, we first extend the GW spectra in the low frequency domain by appending a `TaylorT1` post-Newtonian waveform [118] to that of our

GRMHD simulations to cover the earlier inspiral phase. As in [119], the hybrid waveform is obtained by minimizing

$$\int_{t_i}^{t_f} dt [(h_+^{\rm NR} - h_+^{\rm PN})^2 + (h_\times^{\rm NR} - h_\times^{\rm PN})^2]^{1/2}, \quad (11)$$

using as free parameters the initial PN phase, amplitude, and orbital angular frequency. In all cases, the integration range was chosen to be between $t_i \approx 100\,M$ and $t_f \approx 600\,M$. The right panel of Fig. 3 shows the spectra of the GWs of the dominant mode $(l, m) = (2, 2)$ at a source distance of 50 Mpc, along with the aLIGO (dashed line) and the Einstein Telescope (dotted line) noise curves of configurations in [58] for the cases listed in Table III.

Consistent with previous results (see e.g., [120–122]), we note that the GW spectrum has at least four main frequencies (oscillation modes) associated with the fluid motion during the postmerger phase, which depend strongly on the compactness of the stars, as well as the seed magnetic field (see Table IV). As shown in Fig. 3, these oscillation modes are only present in middle- and long-lived HMNSs. In the short-lived HMNS and prompt collapse cases, most of the matter ($\gtrsim 99\%$ of the total rest-mass of the system; see inset in Fig. 9) is swallowed by the BH in less than 2.5 ms, and hence the oscillations in the spectra are associated with the quasinormal modes of the nascent BH.

The frequency of the f_{2-0} mode, which is produced by a nonlinear interaction between the quadrupole and quasiradial modes [120], depends strongly on the NS compactness and is roughly independent of the magnetic field (see Table IV). We also find that this mode is consistent within $\lesssim 6\%$ with the "universal" behavior associated with the compactness described by the fitting formula [Eq. (1)] in [120]. By contrast, we observe that in most of the cases, the magnetic field damps the amplitude and the frequency of the $f_{\rm spiral}$ mode, which has been associated to the

interaction between the two stellar cores rotating about each other right after merger. In particular, $f_{\rm spiral}$ peaks ~ 87 Hz earlier in H4M2.8P than in H4M2.8H. This suggests that magnetic viscosity tends to accelerate the merger of the two stellar cores. This peak frequency shows a large deviation ($\lesssim 17\%$) from the fitting formula [Eq. (2)] in [120]. On the other hand, the $f_{\rm peak}$ mode, which is related to the rotation of the nonaxisymmetric HMNS, rises $\sim 30 - 150$ Hz in the magnetized cases beyond those in the unmagnetized ones. This behavior is consistent with the rotation profiles of the HMNS remnants displayed in Fig. 8. We also observe that this mode is consistent to within $\lesssim 12\%$ with the fitting formula [Eq. (3)] in [120]. Finally, the f_{2+0} mode in all the unmagnetized case peaks earlier than that in the magnetized cases. Remarkably, this peak is highly affected by the pulsar-like magnetic field (see Table IV). In particular, f_{2+0} in SLyM2.7H peaks ~ 160 Hz earlier than that in SLyM2.7P. These results suggest that the magnetic field introduces a degeneracy with the EOS: two different EOSs may potentially peak at the same frequency due to magnetic effects. These results imply that magnetic effects should be taken into account to constrain the EOS.

According the classification of the postmerger dynamics and GW spectra for transient remnants discussed in [120], all our transients are Type III. In these cases, the dominant secondary peak in the GW spectrum is $f_{\rm spiral}$, while f_{2-0} is very weak (see right panel in Fig. 3) due to low-amplitude radial oscillations of the two NS cores rotating about each other after merger.

Finally, we probe whether the magnetic field leaves any detectable imprints on the GWs that can be measured by the current or future GW detectors. For this purpose, we compute the match function $\mathcal{M}_{\rm GW}$ [57]

$$\mathcal{M}_{\rm GW} = \max_{(\phi_c, t_c)} \frac{\langle h_1 | h_2(\phi_c, t_c) \rangle}{\sqrt{\langle h_1 | h_1 \rangle \langle h_2 | h_2 \rangle}}, \quad (12)$$

between two given waveforms. The maximization is taken over a large set of phase shifts ϕ_c and time shifts t_c. Here $\langle h_1 | h_2 \rangle$ denotes the noise-weighted inner product

$$\langle h_1 | h_2 \rangle = 4{\rm Re} \int_0^\infty \frac{\tilde{h}_1(f) \tilde{h}_2^*(f)}{S_h(f)} df, \quad (13)$$

where $h = h_+ - i h_\times$, $\tilde{h}$ is the Fourier transform of the strain amplitude $\sqrt{\tilde{h}_+(f)^2 + \tilde{h}_\times(f)^2}$ of the dominant mode $(l, m) = (2, 2)$, and $S_h(f)$ is the noise curve of a given detector [58]. As discussed on [57], the value of the match function at which waveforms can potentially be distinguishable depends on the SNR of the waveforms. For a SNR of 15, signals can be indistinguishable if $\mathcal{M}_{\rm GW} \gtrsim 0.9978$, or for a SNR of 25, if the match is larger than 0.9992. For the SLy binaries, those whose three main

TABLE IV. Main spectral frequencies (in Hz) of the dominant mode h_+^{22} for NSNS undergoing delayed collapse (see Table III). Binaries whose merger outcome last $\lesssim 2.5$ ms do no exhibit peak frequencies (see right panel in Fig. 3).

Model	$\mathcal{C}$	f_{2-0}	$f_{\rm spiral}$	$f_{\rm peak}$	f_{2+0}
Γ2M2.8H	0.140	1178	1680	2027	2425
Γ2M2.8P	0.140	1192	1656	2065	2478
H4M2.8H	0.155	1722	2384	2691	3498
H4M2.8I	0.155	1730	2284	2751	3646
H4M2.8P	0.155	1752	2297	2768	3760
SLyM2.6H	0.169	2288	2866	3341	4450
SLyM2.6P	0.169	2301	2899	3404	4458
SLyM2.7H	0.175	2364	2855	3744	4558
SLyM2.7I	0.175	2352	2803	3714	4567
SLyM2.7P	0.175	2378	2807	3930	4718

spectral frequencies peak above the aLIGO sensitive curve (see top right panel in Fig. 3), we find that at distance of 50 Mpc the match function is: (i) $\mathcal{M}_{GW} = 0.9811$ between SLyM2.7H and SLyM2.7I; (ii) $\mathcal{M}_{GW} = 0.9876$ between SLyM2.7I and SLyM2.7P; and (iii) $\mathcal{M}_{GW} = 0.9708$ between SLyM2.7H and SLyM2.7P with a SNR of ~ 1.2 and ~ 3.2 for KAGRA and aLIGO, respectively, or with a SNR of ~ 30 at a distance of ~ 2 Mpc for KAGRA or of ~ 6.0 Mpc for aLIGO, given their current sensitivity [58]. We recall that GW170817, the closest GW signal detected to date, had a luminosity distance of 40^{+8}_{-14} Mpc [1]. Current based-ground GW detectors are unlikely to observer the imprints of the magnetic field on the GW. However, using the expected sensitivity curve for the Einstein Telescope [1], at distance of 50 Mpc we find the same $\mathcal{M}_{GW}$ but with a SNR of ~ 30, and so it can easily observe these imprints. Similar results are found for the H4 and $\Gamma = 2$ binaries. Next generation of GW detectors are thus required to measure the magnetic field imprints on the gravitational radiation at the expected NSNS merger distances.

IV. CONCLUSIONS

A plethora of new GW observations from compact binary mergers is changing our understanding of the Universe at an unprecedented rate. However, these observations have some limitations: (i) source localizations are $\gtrsim 20$ deg^2 (see e.g., [123,124]), preventing identification of the source environment; (ii) the merger of low-mass compact binaries cannot be detected by current ground-based detectors, preventing our determination of their final fates; (iii) GW signals contain uncertainties in the individual masses and spins of the binary companions, etc. However, the coincident detection of GWs with electromagnetic counterparts across the EM spectrum are useful in overcoming some of these limitations. In particular, the detection of GW170817 along with its EM counterparts enabled us to address several long-standing issues: the central engines that power sGRBs, the discovery of off-axis afterglows, the unambiguous identification of a kilonova (AT2017gfo) and the production of heavy elements [1,3,17–19]. GW170817 also demonstrated that to interpret new observations and, in particular, to apply them to understand the physics of matter under extreme conditions, it is crucial to employ results from theoretical modeling.

To understand the physical processes that trigger the emergence of incipient jets, the role of magnetic fields in the dynamical ejection of matter, and the features of GWs from NSNS mergers, we surveyed magnetized NSNS configurations that undergo merger followed by either delayed or prompt collapse to a BH. The binary companions are irrotational stars modeled using a piecewise polytropic implementation of the representative nuclear EOSs SLy and H4, as in [43]. The stars were endowed with an initially poloidal and dynamically weak magnetic field

that was either confined to the stellar interior or protruding from the interior into the exterior, as in typical pulsars.

Consistent with [7,8], we found that jets launched by BH + disks originate only from NSNSs mergers that form HMNS remnants that undergo delayed collapse. This conclusion is independent of the EOS or the magnetic field geometry. This last result may differ from BHNS mergers, where a jet is launched only when the NSs are suitably magnetized with a pulsarlike interior + exterior magnetic field [9].

We noticed that the EOS have a strong impact on the time delay Δt_{jet} between the GW peak amplitude and the jet launching. We observed that the closer the total mass of the binary is to the threshold value for prompt collapse, the shorter Δt_{jet}. We also found that this time strongly depends on the initial extend of the seed magnetic field. The magnetic energy $\mathcal{M}$ in BH + disk remnants whose progenitors are initially endowed with a pulsarlike interior + exterior magnetic field is a factor of ~ 20 larger than in those endowed with a magnetic field confined to the stellar interior. As $\mathcal{M}$ is not enhanced after BH formation, the remnant in the latter requires more time for magnetic pressure gradients to overcome the ram-pressure of the fall-back debris and launch an incipient jet. The lifetime of the jets [$\Delta t \sim 92$–150 ms] and their outgoing Poynting luminosities [$L_{EM} \sim 10^{52\pm1}$ erg/s] are consistent with the sGRB engine lifetime [49–52], as well as with the BZ mechanism for launching jets and their associated Poynting luminosities [39]. The luminosities and BH accretion rates also lie within the rather narrow "universal" range of values predicted in [112] for BH + disk + jet systems formed from compact binary mergers containing magnetized NSs. These results suggests that incipient jets are typically the final outcome of magnetized NSNS undergoing delayed collapse to a BH. Notice that in [59], we discussed the evolution of Γ2M2.8 in full 3D (no symmetries), and found that the remnant launches a magnetically driven jet at roughly the same time as that in the equatorial evolution. In addition, we found that the physical parameters of the BH + disk system, such as mass of the accretion disk, BH spin, etc., are in both cases roughly the same. These results imply that equatorial symmetry does not play any role in the final outcome of the binary merger. As magnetic instabilities cannot be affected by the EOS, we expect our current results to hold in full 3D.

We also observed that the dynamical ejection of matter amounts to $M_{esc} \sim 10^{-4}$–10^{-2} $M_\odot$ and is strongly affected by the EOS. In particular we found that: (i) the softer the EOS, the larger the amount of matter ejected following the NSNS merger. Specifically, the ejecta in SLyM2.7P is a factor of ~ 3 larger than that in H42.8P (see Table III for other cases); (ii) the ejecta can be up to a factor of ~ 8 larger in magnetized NSNS mergers than that in unmagnetized ones. It has been suggested that the magnetic field lines of a rotating compact object may accelerate fluid elements due

to a magnetocentrifugal mechanism [53]. These combined results suggest that GRMHD studies are required to fully explain kilonova signals from GW170817-like events. We used an analytical model [54] to compute the peak luminosity, rise time and effective temperature of the potential kilonova. We found that the bolometric luminosity is $L_{knova} = 1040.6 \pm^{0.5}$ erg/s with rise times of $\tau_{peak} \sim$ 0.4–5.1 days and effective temperature of $\sim 10^{3.5}$ K. We note that this temperature can be translated in a peak wavelength $\lambda_{peak} = 1.35 \times 10^3$ nm$(T_{peak}/10^{3.33}$ K$)^{-1}$ [54], and so $\lambda_{peak} \sim 730$–1830 nm. This EM radiation can be detected with current or planned telescopes [55,56].

Finally, we probed whether the gravitational waveforms contain measurable imprints of the seed magnetic field. We extended the GW spectra in the low frequency domain by appending a `TaylorT1` post-Newtonian waveform to that of our numerical simulations. We found that the magnetic field damps the amplitude and shifts the frequency of the main oscillations modes of the transient HMNS. These two effects introduce a degeneracy with the EOS, since two different EOSs may have peaks at the same frequency due to magnetic effects, and so magnetic fields should be taken into account to constrain the EOS. In addition, we computed the match function between waveforms from systems with the same EOS but different magnetic field content and initial geometry. We found that at distance of 50 Mpc only the next generation of based-ground GW detectors, such as the Einstein Telescope, can observe imprints of the magnetic field on the GWs. Movies and additional 3D visualizations highlighting our simulations can be found at [125].

[1] B. P. Abbott *et al.* (Virgo, LIGO Scientific Collaborations), Phys. Rev. Lett. **119**, 161101 (2017).

[2] A. von Kienlin, C. Meegan, and A. Goldstein, GRB Coordinates Network, Circular Service, No. 21520, #1 (2017), 1520, 2017.

[3] V. Savchenko *et al.*, Astrophys. J. **848**, L15 (2017).

[4] R. Narayan, B. Paczynski, and T. Piran, Astrophys. J. Lett. **395**, L83 (1992).

[5] D. Eichler, M. Livio, T. Piran, and D. N. Schramm, Nature (London) **340**, 126 (1989).

[6] B. Paczynski, Astrophys. J. **308**, L43 (1986).

[7] M. Ruiz, R. N. Lang, V. Paschalidis, and S. L. Shapiro, Astrophys. J. **824**, L6 (2016).

[8] M. Ruiz and S. L. Shapiro, Phys. Rev. D **96**, 084063 (2017).

[9] V. Paschalidis, M. Ruiz, and S. L. Shapiro, Astrophys. J. **806**, L14 (2015).

[10] M. Ruiz, S. L. Shapiro, and A. Tsokaros, Phys. Rev. D **98**, 123017 (2018).

[11] B. P. Abbott *et al.* (LIGO Scientific, Virgo Collaborations), Phys. Rev. Lett. **121**, 161101 (2018).

[12] D. Radice, A. Perego, F. Zappa, and S. Bernuzzi, Astrophys. J. **852**, L29 (2018).

[13] B. Margalit and B. D. Metzger, Astrophys. J. **850**, L19 (2017).

[14] M. Ruiz, S. L. Shapiro, and A. Tsokaros, Phys. Rev. D **97**, 021501 (2018).

[15] L. Rezzolla, E. R. Most, and L. R. Weih, Astrophys. J. **852**, L25 (2018).

[16] M. Shibata, E. Zhou, K. Kiuchi, and S. Fujibayashi, Phys. Rev. D **100**, 023015 (2019).

[17] P. S. Cowperthwaite *et al.*, Astrophys. J. **848**, L17 (2017).

[18] M. M. Kasliwal *et al.*, Science **358**, 1559 (2017).

[19] S. J. Smartt *et al.*, Nature (London) **551**, 75 (2017).

[20] B. P. Abbott *et al.* (LIGO Scientific, Virgo, 1M2H, Dark Energy Camera GW-E, DES, DLT40, Las Cumbres Observatory, VINROUGE, MASTER Collaborations), Nature (London) **551**, 85 (2017).

[21] T. Dietrich, M. W. Coughlin, P. T. H. Pang, M. Bulla, J. Heinzel, L. Issa, I. Tews, and S. Antier, Science **370**, 1450 (2020).

[22] B. Paczyński, in *Texas/PASCOS '92: Relativistic Astrophysics and Particle Cosmology*, edited by C. W. Akerlof and M. A. Srednicki (Annals of the New York Academy of Sciences, New York, 1993), Vol. 688, p. 321.

[23] S. Mao and I. Yi, Astrophys. J. **424**, L131 (1994).

[24] C. A. Meegan, R. D. Preece, and T. Koshut, *Gamma-Ray Bursts, 4th Hunstville Symposium*, American Institute of Physics Conference Series Vol. 428 (1998), https://ui .adsabs.harvard.edu/abs/1998AIPC..428.....M.

[25] T. Kawamura, B. Giacomazzo, W. Kastaun, R. Ciolfi, A. Endrizzi, L. Baiotti, and R. Perna, Phys. Rev. D **94,** 064012 (2016).

[26] R. Ciolfi, W. Kastaun, B. Giacomazzo, A. Endrizzi, D. M. Siegel, and R. Perna, Phys. Rev. D **95,** 063016 (2017).

[27] L. Rezzolla, B. Giacomazzo, L. Baiotti, J. Granot, C. Kouveliotou, and M. A. Aloy, Astrophys. J. Lett. **732,** L6 (2011).

[28] K. Kiuchi, K. Kyutoku, Y. Sekiguchi, M. Shibata, and T. Wada, Phys. Rev. D **90,** 041502 (2014).

[29] V. Paschalidis, Classical Quantum Gravity **34,** 084002 (2017).

[30] F. Foucart, P. Moesta, T. Ramirez, A. J. Wright, S. Darbha, and D. Kasen, arXiv:2109.00565.

[31] P. Mösta, D. Radice, R. Haas, E. Schnetter, and S. Bernuzzi, Astrophys. J. Lett. **901,** L37 (2020).

[32] R. Popham, S. E. Woosley, and C. Fryer, Astrophys. J. **518,** 356 (1999).

[33] T. Di Matteo, R. Perna, and R. Narayan, Astrophys. J. **579,** 706 (2002).

[34] W.-X. Chen and A. M. Beloborodov, Astrophys. J. **657,** 383 (2007).

[35] W.-H. Lei, B. Zhang, and E.-W. Liang, Astrophys. J. **765,** 125 (2013).

[36] O. Just, M. Obergaulinger, H. T. Janka, A. Bauswein, and N. Schwarz, Astrophys. J. **816,** L30 (2016).

[37] Y.-C. Zou and T. Piran, Mon. Not. R. Astron. Soc. **402,** 1854 (2010).

[38] W.-H. Lei, B. Zhang, X.-F. Wu, and E.-W. Liang, Astrophys. J. **849,** 47 (2017).

[39] R. D. Blandford and R. L. Znajek, Mon. Not. R. Astron. Soc. **179,** 433 (1977).

[40] F. F. Dirirsa (Fermi-LAT Collaboration), Proc. Sci., HEASA2016 (**2017**) 004.

[41] F. Douchin and P. Haensel, Astron. Astrophys. **380,** 151 (2001).

[42] N. K. Glendenning and S. A. Moszkowski, Phys. Rev. Lett. **67,** 2414 (1991).

[43] J. S. Read, B. D. Lackey, B. J. Owen, and J. L. Friedman, Phys. Rev. D **79,** 124032 (2009).

[44] E. Fonseca *et al.*, Astrophys. J. **832,** 167 (2016).

[45] J. Antoniadis *et al.*, Science **340,** 6131 (2013).

[46] H. T. Cromartie *et al.* (NANOGrav Collaboration), Nat. Astron. **4,** 72 (2020).

[47] M. Ruiz, A. Tsokaros, V. Paschalidis, and S. L. Shapiro, Phys. Rev. D **99,** 084032 (2019).

[48] R. Ciolfi, W. Kastaun, J. V. Kalinani, and B. Giacomazzo, Phys. Rev. D **100,** 023005 (2019).

[49] P. Beniamini, R. B. Duran, M. Petropoulou, and D. Giannios, Astrophys. J. Lett. **895,** L33 (2020).

[50] P. N. Bhat *et al.*, Astrophys. J. Suppl. Ser. **223,** 28 (2016).

[51] A. Lien *et al.*, Astrophys. J. **829,** 7 (2016).

[52] D. S. Svinkin, D. D. Frederiks, R. L. Aptekar, S. V. Golenetskii, V. D. Pal'shin, P. P. Oleynik, A. E. Tsvetkova,

M. V. Ulanov, T. L. Cline, and K. Hurley, Astrophys. J. Suppl. Ser. **224,** 10 (2016).

[53] R. D. Blandford and D. G. Payne, Mon. Not. R. Astron. Soc. **199,** 883 (1982).

[54] A. Perego, F. K. Thielemann, and G. Cescutti, r-Process Nucleosynthesis from compact binary mergers, in *Handbook of Gravitational Wave Astronomy*, edited by C. Bambi, S. Katsanevas, and K. D. Kokkotas (Springer, Berlin, Germany, 2021), p. 1, ISBN: 978-981-15-4702-7.

[55] L. D. Matthews *et al.*, Publ. Astron. Soc. Pac. **130,** 015002 (2018).

[56] H.-Y. Chen, P. S. Cowperthwaite, B. D. Metzger, and E. Berger, Astrophys. J. Lett. **908,** L4 (2021).

[57] I. Harry and T. Hinderer, Classical Quantum Gravity **35,** 145010 (2018).

[58] B. P. Abbott *et al.* (LIGO Scientific Collaboration), Classical Quantum Gravity **34,** 044001 (2017).

[59] M. Ruiz, A. Tsokaros, and S. L. Shapiro, Phys. Rev. D **101,** 064042 (2020).

[60] A. Tsokaros, M. Ruiz, S. L. Shapiro, L. Sun, and K. Uryū, Phys. Rev. Lett. **124,** 071101 (2020).

[61] Z. B. Etienne, Y. T. Liu, and S. L. Shapiro, Phys. Rev. D **82,** 084031 (2010).

[62] CactusConfigs, Cactus Machine Configurations, http:// www.cactuscode.org/Documentation/Configurations.html.

[63] E. Schnetter, S. H. Hawley, and I. Hawke, Classical Quantum Gravity **21,** 1465 (2004).

[64] Carpet, Carpet Code homepage, http://www.carpetcode .org/.

[65] M. Shibata and T. Nakamura, Phys. Rev. D **52,** 5428 (1995).

[66] T. W. Baumgarte and S. L. Shapiro, Phys. Rev. D **59,** 024007 (1998).

[67] Z. B. Etienne, J. A. Faber, Y. T. Liu, S. L. Shapiro, K. Taniguchi, and T. W. Baumgarte, Phys. Rev. D **77,** 084002 (2008).

[68] J. G. Baker, J. Centrella, D.-I. Choi, M. Koppitz, and J. van Meter, Phys. Rev. D **73,** 104002 (2006).

[69] B. D. Farris, R. Gold, V. Paschalidis, Z. B. Etienne, and S. L. Shapiro, Phys. Rev. Lett. **109,** 221102 (2012).

[70] Z. B. Etienne, V. Paschalidis, Y. T. Liu, and S. L. Shapiro, Phys. Rev. D **85,** 024013 (2012).

[71] A. Tsokaros, K. Ury, and L. Rezzolla, Phys. Rev. D **91,** 104030 (2015).

[72] A. Tsokaros, K. Uryu, M. Ruiz, and S. L. Shapiro, Phys. Rev. D **98,** 124019 (2018).

[73] T. E. Riley *et al.*, Astrophys. J. Lett. **918,** L27 (2021).

[74] P. T. H. Pang, I. Tews, M. W. Coughlin, M. Bulla, C. Van Den Broeck, and T. Dietrich, Astrophys. J. **922,** 14 (2021).

[75] M. C. Miller *et al.*, Astrophys. J. Lett. **887,** L24 (2019).

[76] A. Tsokaros, M. Ruiz, and S. L. Shapiro, Astrophys. J. **905,** 48 (2020).

[77] M. Shibata and K. Taniguchi, Phys. Rev. D **73,** 064027 (2006).

[78] A. Bauswein, S. Blacker, V. Vijayan, N. Stergioulas, K. Chatziioannou, J. A. Clark, N.-U. F. Bastian, D. B. Blaschke, M. Cierniak, and T. Fischer, Phys. Rev. Lett. **125,** 141103 (2020).

[79] T. W. Baumgarte, S. L. Shapiro, and M. Shibata, Astrophys. J. Lett. **528**, L29 (2000).

[80] A. Bauswein, H. T. Janka, and R. Oechslin, Phys. Rev. D **82**, 084043 (2010).

[81] V. Paschalidis, Y. T. Liu, Z. Etienne, and S. L. Shapiro, Phys. Rev. D **84**, 104032 (2011).

[82] R. Aguilera-Miret, D. Viganò, F. Carrasco, B. Miñano, and C. Palenzuela, Phys. Rev. D **102**, 103006 (2020).

[83] K. Kiuchi, P. Cerd-Durn, K. Kyutoku, Y. Sekiguchi, and M. Shibata, Phys. Rev. D **92**, 124034 (2015).

[84] Z. B. Etienne, Y. T. Liu, V. Paschalidis, and S. L. Shapiro, Phys. Rev. D **85**, 064029 (2012).

[85] A. Tsokaros, M. Ruiz, V. Paschalidis, S. L. Shapiro, and K. Uryū, Phys. Rev. D **100**, 024061 (2019).

[86] J. Thornburg, Classical Quantum Gravity **21**, 743 (2004).

[87] O. Dreyer, B. Krishnan, D. Shoemaker, and E. Schnetter, Phys. Rev. D **67**, 024018 (2003).

[88] M. Ruiz, R. Takahashi, M. Alcubierre, and D. Nunez, Gen. Relativ. Gravit. **40**, 2467 (2008).

[89] M. Shibata and K. Hotokezaka, Annu. Rev. Nucl. Part. Sci. **69**, 41 (2019).

[90] D. Radice, A. Perego, K. Hotokezaka, S. A. Fromm, S. Bernuzzi, and L. F. Roberts, Astrophys. J. **869**, 130 (2018).

[91] B. P. Abbott et al. (LIGO Scientific, Virgo Collaborations), Astrophys. J. Lett. **850**, L39 (2017).

[92] B. Côté et al., Astrophys. J. **855**, 99 (2018).

[93] B. D. Farris, Y. T. Liu, and S. L. Shapiro, Phys. Rev. D **81**, 084008 (2010).

[94] N. I. Shakura and R. A. Sunyaev, Astron. Astrophys. **24**, 337 (1973), http://adsabs.harvard.edu/abs/1973A%26A... .24..337S.

[95] R. F. Penna, J. C. McKinney, R. Narayan, A. Tchekhovskoy, R. Shafee, and J. E. McClintock, Mon. Not. R. Astron. Soc. **408**, 752 (2010).

[96] Z. B. Etienne, V. Paschalidis, and S. L. Shapiro, Phys. Rev. D **86**, 084026 (2012).

[97] T. Sano, S.-i. Inutsuka, N. J. Turner, and J. M. Stone, Astrophys. J. **605**, 321 (2004).

[98] H. Shiokawa, J. C. Dolence, C. F. Gammie, and S. C. Noble, Astrophys. J. **744**, 187 (2012).

[99] B. Giacomazzo, L. Rezzolla, and L. Baiotti, Phys. Rev. D **83**, 044014 (2011).

[100] M. Shibata and K. Uryu, Prog. Theor. Phys. **107**, 265 (2002).

[101] M. Shibata, K. Taniguchi, and K. Uryu, Phys. Rev. D **68**, 084020 (2003).

[102] M. Shibata and K. Taniguchi, Phys. Rev. D **73**, 064027 (2006).

[103] R. Ciolfi, S. K. Lander, G. M. Manca, and L. Rezzolla, Astrophys. J. Lett. **736**, L6 (2011).

[104] P. D. Lasky, B. Zink, K. D. Kokkotas, and K. Glampedakis, Astrophys. J. Lett. **735**, L20 (2011).

[105] L. Sun, M. Ruiz, and S. L. Shapiro, Phys. Rev. D **99**, 064057 (2019).

[106] K. Kiuchi, K. Kyutoku, Y. Sekiguchi, and M. Shibata, Phys. Rev. D **97**, 124039 (2018).

[107] K. Kiuchi, K. Kyutoku, and M. Shibata, Phys. Rev. D **86**, 064008 (2012).

[108] K. S. Thorne, R. H. Price, and D. A. Macdonald, The Membrane Paradigm (Yale University Press, New Haven, 1986).

[109] S. S. Komissarov, Mon. Not. R. Astron. Soc. **326**, L41 (2001).

[110] J. C. McKinney and C. F. Gammie, Astrophys. J. **611**, 977 (2004).

[111] N. Vlahakis and A. Königl, Astrophys. J. **596**, 1080 (2003).

[112] S. L. Shapiro, Phys. Rev. D **95**, 101303 (2017).

[113] Y. Li, B. Zhang, and H.-J. L, Astrophys. J. Suppl. Ser. **227**, 7 (2016).

[114] B. D. Metzger, Living Rev. Relativity **20**, 3 (2017).

[115] L.-X. Li and B. Paczynski, Astrophys. J. Lett. **507**, L59 (1998).

[116] M. Tanaka and K. Hotokezaka, Astrophys. J. **775**, 113 (2013).

[117] J. Barnes and D. Kasen, Astrophys. J. **775**, 18 (2013).

[118] P. Ajith, M. Boyle, D. A. Brown, S. Fairhurst, M. Hannam, I. Hinder, S. Husa, B. Krishnan, R. A. Mercer, F. Ohme, C. D. Ott, J. S. Read, L. Santamaria, and J. T. Whelan, arXiv:0709.0093.

[119] M. Ruiz, V. Paschalidis, A. Tsokaros, and S. L. Shapiro, Phys. Rev. D **102**, 124077 (2020).

[120] A. Bauswein and N. Stergioulas, Phys. Rev. D **91**, 124056 (2015).

[121] S. Vretinaris, N. Stergioulas, and A. Bauswein, Phys. Rev. D **101**, 084039 (2020).

[122] K. Takami, L. Rezzolla, and L. Baiotti, Phys. Rev. D **91**, 064001 (2015).

[123] R. Abbott et al. (LIGO Scientific, Virgo Collaborations), Phys. Rev. X **11**, 021053 (2021).

[124] B. P. Abbott et al. (LIGO Scientific, Virgo Collaborations), Phys. Rev. X **9**, 031040 (2019).

[125] 3d visualizations and movies, http://research.physics .illinois.edu/cta/movies/NSNS_2021.